Dalton Transactions

PAPER

View Article Online
View Journal | View Issue

Cite this: *Dalton Trans.*, 2015, **44**, 3159

A relationship between structural and electronic order–disorder effects and optical properties in crystalline TiO_2 nanomaterials†

E. Silva Junior,*[a] F. A. La Porta,[a] M. S. Liu,[b] J. Andrés,[c] J. A. Varela[a] and E. Longo[a]

The focus of this paper is on the analysis of the structural and electronic order–disorder effects at long, medium and short ranges of titanium dioxide (TiO_2) nanoparticles synthesized by the sol–gel process followed by the microwave-assisted solvothermal (MAS) method at low temperatures and short reaction times. X-ray diffraction (XRD), Rietveld refinement, micro-Raman (MR) spectroscopy, transmission electron microscopy (TEM) and X-ray spectroscopy (EDX) were used to characterize the TiO_2 nanoparticles. Optical properties were investigated by ultraviolet-visible (UV-vis) and photoluminescence (PL) measurements performed at room temperature. XRD and Rietveld refinement confirmed the presence of the anatase and brookite phases; nonetheless anatase is the major phase. The X-ray photoelectron spectroscopy (XPS) analysis revealed the presence of only Ti^{4+} but the nonstoichiometry revealed that TiO_2 NPs contain defects assigned to oxygen vacancies that lead to structural and electronic order–disorder effects observed by band gap narrowing and PL wide band emission. These intermediary energy levels (shallow and deep levels) created within the band gap act as acceptors/donors of electrons and recombination centers. The oxygen vacancies (V_O^x, $V_O^{\bullet}$ and $V_O^{\bullet\bullet}$) responsible by degree of structural order–disorder are related to distortions (*tilts*) on the [TiO_6] octahedron and changes in the bond lengths and bond angles between oxygen and titanium atoms that gave rise to new species of cluster makers such as [TiO_6]′, [$TiO_5{\cdot}V_O^x$], [$TiO_5{\cdot}V_O^{\bullet}$] and [$TiO_5{\cdot}V_O^{\bullet\bullet}$]. This structural transformation is consistent with a redistribution of electron density from highly ordered [TiO_6]^x clusters which form distorted [TiO_6]′ as well as complex [$TiO_5{\cdot}V_O^x$], [$TiO_5{\cdot}V_O^{\bullet}$] and [$TiO_5{\cdot}V_O^{\bullet\bullet}$] clusters assigned to oxygen vacancies which were understood as displacements in the oxygen atoms' position in the bond lengths (Ti–O).

Received 21st October 2014,
Accepted 11th December 2014

DOI: 10.1039/c4dt03254c

www.rsc.org/dalton

Introduction

Titanium dioxide (TiO_2) is a versatile material which is utilized in a range of technological applications which embrace areas ranging from photovoltaic cells and photocatalysis to gas sensors.[1–4] TiO_2 properties depend strongly on the particle size, crystal structure, morphology and crystallinity.[5–7] Natural polymorphs of titania (TiO_2) include rutile (*P*42/*mnm*), anatase (*I*42/*amd*) and brookite (*Pcab*) with wide band gaps of 3.02, 3.20 and 2.96 eV, respectively. Each phase has unique physical properties, and phase transitions are dependent upon many factors such as particle size, morphology, pH, *etc.*[8] Phase stability and phase transformation kinetics are substantially different in nanosized solids as compared to their bulk counterparts. A typical example of this phenomenon is that TiO_2 nanoparticles (NPs) have a stable rutile phase in bulk materials; however, the anatase phase becomes stable in TiO_2 NPs at a size smaller than 14 nm.[9] The theoretical background to this phenomenon has been provided based on *ab initio* density functional theory (DFT) calculations.[10]

From a structural point of view, all three crystal structures consist of six-fold coordinated Ti atoms made up of [TiO_6] clusters and three-fold coordinated O atoms which share either edges or corners. The [TiO_6] octahedron can be considered as constituent clusters of TiO_2 but with different arrangements of neighboring and distorted [TiO_6] cluster-sharing oxygen atoms where they form three different crystallographic structures.[11–16] In this family, [TiO_6] octahedral clusters, in particular, exhibit marked structural flexibility and the structural distortion from rotation/tilting does not disrupt the corner-sharing connectivity in these frameworks. Galynska

[a]*LIEC, Instituto de Química, Universidade Estadual Paulista, P.O. Box 355, CEP 14801-907 Araraquara, SP, Brazil. E-mail: euripedessj@gmail.com; Fax: +55 16 3301-9691; Tel: +55 16 3301-9892*
[b]*Instituto de Física de São Carlos, Universidade de São Paulo, P.O. Box 369, 13560-970 São Carlos, SP, Brazil*
[c]*Department of Physical and Analytical Chemistry, Universitat Jaume I, Castelló de la Plana, 12071, Spain*
†Electronic supplementary information (ESI) available. See DOI: 10.1039/c4dt03254c

and Persson[17] carried out quantum chemical calculations to show that the different TiO_2 forms of the three polymorphs can be clearly distinguished based on structural characteristics associated with the local bonding environment of the constituent atoms.

As basic units, electronic structures of these clusters are drastically affected by structural order–disorder effects, and control of these lattice disorders in NPs is essential for developing nanomaterials tailored to specific optical properties and further applications. It is only by probing these phenomena locally that we can hope to link the structure and functionality of materials and thus open pathways for predictive modelling and synthesis. Very recently, Landmann and co-workers[18] used the distorted $[TiO_6]$ cluster and partial loss of this octahedral coordination as fingerprints of order and disorder in the electronic and optical properties of crystalline and amorphous TiO_2.

The properties, size and morphology of the as-synthesized nanomaterials are highly dependent on reaction conditions. TiO_2 nanostructures with various morphologies and sizes have been successfully synthesized using a variety of methods.[12,19] In comparison with other methods, the sol–gel technique has advantages such as controllability, reliability and reproducibility which results in high quality and high purity materials.[20,21] However, the polycondensation reaction of the sol–gel method materials results in an amorphous phase or a low degree of crystallinity.[21] Thus, it is necessary to perform a crystallization procedure, *e.g.* heat treatment by calcining, hydrothermal or solvothermal processes.

Among the modern techniques of synthetic chemistry, the microwave-assisted solvothermal (MAS) method is beneficial in all areas.[22a,b] In particular, the use of microwave heating for the preparation of semiconductor nanomaterials has been employed due to its advantages over other synthetic methods. Primarily, the application of microwave irradiation on chemical transformations has been demonstrated to enhance reaction rates and cost effectiveness as well as to improve material quality and size distributions in nanomaterials and obtain cleaner reactions as compared to conventional routes.[23–28] Because the mechanism and the microwave effects with synthesis are not well understood, this area is an open research field.[29–31] However, the MAS process promotes a nucleation–dissolution–recrystallization mechanism that is an order–disorder process which facilitates a non-classical crystallization process.[32]

In this context, an understanding of the formation of energy gaps is directly related to the nature of electronic and optical properties. The novelty of this work lies in the possibility that TiO_2 might be used as sources of blue and red light in light emitting devices in the future. Therefore, it is challenging and of scientific interest to obtain deeper insights into how structural and electronic properties can be related to short- and/or long-range order–disorder effects to explain the optical properties of TiO_2 NPs obtained by a sol–gel process followed by the MAS method. To accomplish this deeper insight, XRD, Rietveld refinement, MR spectroscopy, TEM and EDX analyses have been employed while optical properties were investigated by UV–Vis absorption and PL measurements. In addition, effects as well as the influence of the microwave heating using the synthetic process are reported.

Experimental

Materials and methods

All chemicals were used as obtained without further purification. Titanium(IV) isopropoxide (97% purity, Aldrich), ethyl alcohol anhydrous (99% purity, Fluka), hydrochloric acid (36.5–38 wt%, Merck) and deionized water (Milli-Q ultra-pure; resistivity of 18.2 M cm^{-1}) were maintained in a molar ratio of 1 : 20 and 0.75 : 4, respectively.

TiO_2 NPs were obtained by a two-step synthetic route based on the sol–gel process followed by the MAS treatment as follows: first, hydrochloric acid (3.11 mL) was added to ethyl alcohol (75 mL) with stirring for 15 min. Then titanium(IV) isopropoxide (14.8 mL) was added using an ultrasonic cleaner for agitation for 3 min; a slightly yellowish transparent solution was produced which was stirred for 1 h. To promote the hydrolysis of metal alkoxide, deionized water (3.6 mL) was added to this solution while using an ultrasonic cleaner for 3 min, which resulted in a clear solution. The clear solution (linear polymer chains dispersed in the solvent) was placed in a sealed 100 mL Teflon®autoclave and loaded into a non-commercial microwave oven which was operated at 2.45 GHz and 850 W of power. This system was processed at 120 °C under constant pressure (approximately 3.0 bar) for 2, 8 and 32 min with a heating rate of 10 °C min^{-1}. After heat treatment, a milky solution of TiO_2 NPs was formed which was characterized by the formation of particulate gels. The nanoparticulate gels were dried at 50 °C to obtain xerogels which were subsequently crushed in a mortar to obtain a fine powder; the powder was calcined in a muffle furnace at 380 °C for 12 h to remove organic matter.

Characterization

The structural analysis of the synthesized TiO_2 was performed by XRD using a Rigaku-DMax 2500PC (Japan) diffractometer at 40 kV and 150 mA with Cu-Kα radiation (λ = 1.5406 Å). The Rietveld routine was performed in the 2θ range from 10° up to 110° in a step-scanning mode with a step width of 0.02° s^{-1} and a fixed time of 1 s. The divergence slit used was fixed at 1°, and the receiving slit was established at 0.3 mm. The Rietveld refinement method[33] was conducted using the General Structure Analysis System (GSAS) software designed by Larson and Von Dreele.[34] The peak profile function was modeled using a convolution of the pseudo-Voigt with the asymmetry function described by Finger and Cox.[35] ICSD CIF numbers 24276[36] and 31122[37] (ICSD – Inorganic Crystal Structure Database) were employed to obtain the best fit between the theoretical profile and the measured profiles.

MR spectroscopy data were recorded using a T-64000 Jobin-Yvon triple monochromator coupled to a CCD detector. MR

spectra were obtained using a 632.81 nm wavelength of an argon ion laser with its maximum output power maintained at 8 mW. A 50 μm lens was used to prevent powder overheating, and MR data were taken with 30 s of acquisition time.

Morphologies were investigated using TEM and EDX, and selected area diffraction (SAED) patterns were recorded on a JEOL 2100 transmission electron microscope operated at 200 kV. In the sample preparation for the TEM technique, the obtained powders were first dispersed in ethanol using an ultrasonic bath for 20 min, and then the suspensions were deposited on copper grids *via* fast immersion. The compositional analysis as well as the mapping of elements in analyzed samples was performed using EDX.

UV-vis spectra were recorded employing a Cary 5G spectrophotometer (Varian, USA) in diffuse reflectance mode. E_{gap} values were calculated using a method proposed by Kubelka and Munk,[38] where this energy is associated with diffuse reflectance measurements to estimate E_{gap} values with good accuracy (see ESI†). XPS was employed to determine the surface chemical composition and the oxidation states of the TiO_2 NPs. XPS spectra were recorded employing a UNI-SPECS UHV system operated at pressures less than 5×10^{-7} Pa with an Mg-K_α line ($h\nu$ = 1253.6 eV) ionization source and the pass energy of the analyzer set to 10 eV. The inelastic noise of the high resolution spectrum for O 1s, Ti 2p, and C 1s was subtracted by the Shirley method.[39] The compositional atomic percentages of the surface layer (<5 nm) were determined by relative proportions of the spectrum areas revised by means of atomic sensitivity factors using a hydrocarbonate component corresponding to the C 1s peak position around 284.95 eV as the reference point. The XPS spectrum was deconvoluted using a Voigt function (Gauss 70% and Lorentz 30%) and the peak positions were determined within ±0.1 eV accuracy. PL spectra were measured in pellets at room temperature under an air atmosphere using a Monospec 27 monochromator (Thermal Jarrel Ash, USA) coupled to an R446 photomultiplier (Hamamatsu Photonics, Japan). A krypton ion laser (Coherent Innova 90 K, USA) ($h\nu$ = 350 nm) was employed as an excitation source; its maximum output power was maintained at 500 mW and a maximum power of 40 mW on the sample after passing through an optical chopper.

Results and discussion

X-ray and Rietveld refinement data analyses

Long-range structural order is determined by XRD patterns which elucidate that the lattices of the TiO_2 NPs are formed by anatase (space group $I41/amd$ in a D_{4h} symmetry) and brookite (space group $Pcab$ in a D_2 symmetry) which were indexed and are in good agreement with ICSD CIF no. 24276 and CIF no. 31122. Fig. 1 displays the XRD patterns performed with the Rietveld routine. The weak peak at the diffraction position at $2\theta = 30.65°$ is assigned to the brookite orthorhombic structure for the plane (121) while a strong peak at $2\theta = 25.32°$ relating to the plane (101) of the tetragonal anatase. The other peaks

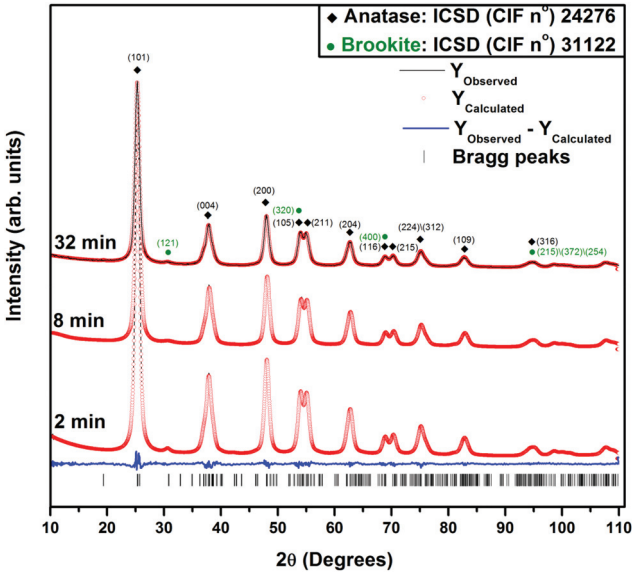

Fig. 1 Rietveld refinement data of TiO_2 nanoparticles processed *via* the microwave-assisted solvothermal method in 2, 8 and 32 minutes at 120 °C.

diffracted were also indexed; however due to the broadening of the peaks, a phenomenon usually found in systems composed of nanoparticles,[40] and the proximity of the diffracted peak position of some planes in both anatase (A) and brookite (B) phases, certain peaks might be ascribed to more than one plane. So, the other planes indexed were (101) A, (004) A, (200) A, (105) A or (320) B, (211) A, (204) A, (116) A or (400) B, (215) A, (224) A or (312) A, (217) A, (109) A and (316) A or (125)/(372)/(254) B. All planes indexed as well as their *d*-spacing, diffraction peak position (2θ) and intensity are displayed in detail in Table S1 (see ESI†). Therefore, the TiO_2 NPs are formed by two crystallographic structures, anatase and brookite, which the anatase phase is the major structural constituent in the TiO_2 NP lattice.

Structural parameters were obtained from Rietveld refinements of XRD data and are displayed in Table 1. The Rietveld refinement method was employed to understand whether there are any differences in the structural arrangements of TiO_2 NPs processed by MAS. The fit was performed using the least-squares approach by minimizing the sum of squares of differences between the theoretical values and the observed data.[41a] The fit is conducted assuming the hypothesis that the reflections that contribute to the profile can be simulated with the selected profile function.[41b] Thus, the intensity value calculated in this process does not include the calculation of structural factors but is achieved by refining the values related to parameters of the peak-shape function selected for each reflection *hkl*, where the theoretical peak profiles are adjusted to converge with the measured profiles.[41c] The uncertainty in the derived weight fractions ascribed to each crystalline or amorphous phase beyond the effects of preferred orientation, primary extinction, and nonlinear detection systems can be minimized using all reflections in a pattern, rather than just

Table 1 Fitting parameters of the Rietveld refinements, lattice parameters and atomic coordinate site occupancy obtained for TiO_2 nanoparticles compared to reported in the ICDS CIF no. 24276 and no. 31122[a]

Crystal structure	Tetragonal $I4_1/amd$ – anatase				Orthorhombic *Pbca* – brookite			
Refinement parameters	χ^2	R_B%	R_{WP}%	wt%	χ^2	R_B%	R_{WP}%	wt%
TiO_2 [b] (nanoparticles)								
2 minutes	0.2749	0.85	4.62	94.07	0.2749	2.59	4.62	5.93
8 minutes	0.2451	0.56	4.41	94.40	0.2451	1.86	4.41	5.60
32 minutes	0.2435	0.88	4.15	91.87	0.2435	0.88	4.15	8.13
Lattice parameters	*a* (Å)	*b* (Å)	*c* (Å)	*V* (Å^3)	*a* (Å)	*b* (Å)	*c* (Å)	*V* (Å^3)
TiO_2 [b]								
2 minutes	3.7856	3.7856	9.5037	136.20	9.1740	5.4490	5.1380	256.84
TiO_2 [b]								
8 minutes	3.78602	3.78602	9.50560	136.25	9.17400	5.44900	5.13800	256.84
TiO_2 [b]								
32 minutes	3.7867	3.7867	9.5033	136.27	9.2020	5.4700	5.2590	264.71
TiO_2 [c]								
ICSD no. 24276	3.7710	3.7710	9.4300	134.10	—	—	—	—
TiO_2 [d]								
ICSD no. 31122	—	—	—	—	9.1740	5.4490	5.1380	256.84

Atomic coordinates titanium and oxygen

TiO_2 [b] (nanoparticles)	Atom	Site	*x*	*y*	*z*	Atom	Site	*x*	*y*	*z*
2 minutes	Ti	4b*(+4)*	0	0.25	0.32500	Ti	8c*(+4)*	0.12890	0.09720	0.86280
	O	8e*(−2)*	0	0.25	0.01305	O	8c*(−2)*	0.00950	0.14910	0.18350
						O	8c*(−2)*	0.23140	0.11100	0.53660
8 minutes	Ti	4b*(+4)*	0	0.25	0.37500	Ti	8c*(+4)*	0.12890	0.09720	0.86280
	O	8e*(−2)*	0	0.25	0.16656	O	8c*(−2)*	0.00950	0.14910	0.18350
						O	8c*(−2)*	0.23140	0.11100	0.53660
32 minutes	Ti	4b*(+4)*	0	0.25	0.37500	Ti	8c*(+4)*	0.10181	0.10117	0.855240
	O	8e*(−2)*	0	0.25	0.16562	O	8c*(−2)*	0.05731	0.13769	0.151230
						O	8c*(−2)*	0.21277	0.14885	0.493450
TiO_2 (bulk-theoretical)	Atoms	Site	*x*	*y*	*z*	Atoms	Site	*x*	*y*	*z*
	Ti	4b*(+4)*	0	0	0.37500	Ti	8c*(+4)*	0.12800	0.09800	0.86300
	O	8e*(−2)*	0	0	0.20800	O	8c*(−2)*	0.00800	0.14700	0.18200
						O	8c*(−2)*	0.22900	0.11000	0.53000

[a] ICSD = International Crystal Structure Database; *a*, *b*, *c* = Lattice parameters; *V* = Unit cell volume. [b] TiO_2 nanoparticles processed by the microwave-assisted solvothermal method in 2, 8 and 32 minutes. [c] TiO_2 anatase bulk (ICSD CIF no. 24276). [d] TiO_2 brookite bulk (ICSD CIF no. 31122).

the strongest ones.[41d] Some criteria to judge the quality adjustments are required and therefore it is necessary to use some well-known indices like *R*-factors or Disagreement Factors (R_p – Profile Factor; R_{wp} – Weighted Profile Factor; R_{exp} – Expected Profile Factor; (*s*) Goodness of Fit Indicator; and χ^2 – Reduced Chi-Square) which inform each cycle, if refinement proceeds satisfactorily and if it can be finalized with high accuracy.[42a] According to the literature[42b,c] the data arising from structural refinements are generally checked by the quality algorithms or *R*-factors. However, the differences between the measured and calculated patterns might be a good way to verify the convergence of the refinement.

In this work, the parameters and coefficients optimized were the scale factor, background (with function type: shifted Chebyshev using 8 terms), sample displacement, Lorentzian coefficient to correct the sample broadening, size-strain (anisotropic no rules), peak cutoff fixed at 3×10^{-4} to adjust the width of the peak base, microstructure, crystal structure, size-strain (anisotropic no rules), profile half-width parameters (*u*, *v*, *w*), lattice parameters (*a*, *b*, *c*), factor occupancy, and atomic site occupancies (Wyckoff).[42c,d] The adjustable parameters related to *R*-factors show good correlation between the simulated theoretical model and experimental data while lattice parameters and unit cell volumes are very close to results published in the literature.[42b,e]

The rapid TiO_2 formation process that governs microwave heating produces significant variations in *a*, *b* and *c* lattice parameter values and unit cell volumes. For TiO_2 NPs synthesized for 32 min, these distortions, stresses and strains yield a larger mass percentage (wt%) of the brookite phase (5.93%, 5.60% and 8.13%) with 94.07%, 94.40% and 91.87% of wt% assigned to the anatase phase, for TiO_2 NPs processed at 2, 8, and 32 minutes, respectively.

A number of variations in atomic position related to O and Ti atoms were observed which were independent of the time process for both anatase and brookite phases. We believe that these variations in atomic positions of atoms can result in the formation of distortions on the [TiO_6] octahedral cluster

networks. Rapid heating with the MAS method causes structural defects due to distortions of the coordination polyhedra which are the nanomaterials' building blocks. This structural transformation is consistent with order–disorder effects in the crystal lattice as well as with redistribution of electron density from ideal [TiO_6] clusters to form distorted [TiO_5] clusters in the lattice. Table 1 shows the atomic position of the oxygen atom in the *z* coordinate of the 8e site which is displaced compared to the bulk coordinates of the anatase phase. For the brookite phase, displacements were observed for Ti and O atoms in the *x*, *y* and *z* coordinates of the 8c sites. We believe that the distortions on the coordination polyhedron are due to these displacements of the Ti and O atoms, and therefore the bond lengths and bond angles in O–Ti–O undergo changes that can generate redistribution of electron density in the crystal lattice.

Micro-Raman analyses

To compare results obtained by XRD, we used Raman spectroscopy to evaluate the phase composition as well as the degree of order–disorder at short range of TiO_2 NPs. The information obtained by Raman scattering has been an excellent tool in the study of the formation of TiO_2 and titanates.[43–49] The information related to the degree of order–disorder in the Raman spectrum is relative to the intensity, width and displacements of vibrational mode peaks.[44,45] Fig. 2 shows MR spectra in the range of 50 cm^{-1} to 1000 cm^{-1} for TiO_2 NPs. Raman bands located around 144, 197, 399, 513, 519 and 639 cm^{-1} correspond to anatase vibrational Raman modes.[44] According to the symmetry group analysis of TiO_2 vibrational spectra, the anatase crystal structure has six Raman active modes ($A_{1g} + 2B_{1g} + 3E_g$); another three modes ($A_{2u} + 2E_u$) are infrared active; and one mode (B_{2u}) is inactive in the Raman or infrared region. For the brookite phase, Raman-active modes are located at around 150, 323, 416 and 636 cm^{-1}, respectively.[46,47] In particular, the width of the most intensive Raman band of brookite located at 154 cm^{-1} can influence the width of the Raman mode of anatase structure at 144 cm^{-1}. The brookite phase must have vibrational mode characteristics with a strong Raman scattering close to 128 (A_{1g}), 153 (A_{1g}), 247 (A_{1g}), 322 (B_1g), 366 (B_{2g}) and 636 cm^{-1} (A_{1g}), while the anatase phase already shows characteristic scattering at 146 (E_g), 396 (B_{1g}), 515 (A_{1g}) and 641 cm^{-1} (E_g).[46,47] The spectrum shown in Fig. 2 reveals that Raman bands of TiO_2 NPs were located at 144.3, 195.2, 394.8, 513.1 and 637.4 cm^{-1}, respectively.

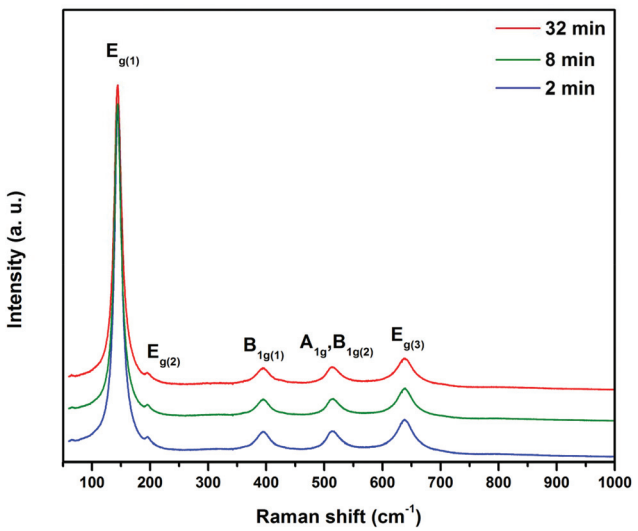

Fig. 2 MR spectra in the range from 50 cm^{-1} to 1000 cm^{-1} for TiO_2 nanoparticles processed in 2, 8 and 32 minutes at 120 °C.

Raman band values for TiO_2 NPs synthesized at 2, 8 and 32 min belong to anatase vibrational modes (E_{g1}, E_{g2}, B_{1g}, A_{1g}, B_{1g}, and E_{g3}).[48] However, the positions of two modes (A_{1g} and B_{1g}) are not well defined in these Raman bands because there is an overlap of two modes and then a wide peak appears. In Raman scattering, the behavior of the dispersion slope from the scattering vector (q) is close to the Brillouin zone center ($q \approx 0$) for a given phonon mode which describes the nature of the association for a modification in the Raman line shape as a function of the crystal size.[49] A decrease in the crystal size facilitates a modification in the Raman line shape (negative slope) as well as a down-shifted or red-shifted Raman peak accompanied by increased broadening while an increase in the crystal size yields an up-shifted or blue-shifted Raman peak accompanied by a decreased broadening.[47,48]

An analysis of Fig. 2 reveals that MR spectra associated with TiO_2 nanoparticles processed in 2, 8 and 32 min are very similar regarding the occurrence of red-shifted and blue-shifted peaks while peak broadening was not noticeable. Therefore, TiO_2 NP crystal sizes are similar or are not capable of facilitating a modification in the Raman line shape. Thus, the presence of only six well defined Raman active modes ($A_{1g} + 2B_{1g} + 3E_g$) suggests that TiO_2 NPs for all synthesis times (2, 8 and 32 min) are ordered at long- and short-range with the anatase structure and there are no vibrational modes relative to other TiO_2 polymorphs. This conclusion is consistent with XRD results shown in Fig. 1.

TEM analyses

Morphologies of the synthesized TiO_2 products were studied by TEM. Fig. 3(a–c) display HR-TEM images taken at higher magnifications. The first objective is to obtain a closer look at how these NPs are positioned on the carbon grid. Under higher magnification, nanocrystal agglomerates are observed and TiO_2 nanoparticles with an average size of approximately 10 nm are observed. This result agrees with the fact that anatase is the most stable structure observed at the nanoscale, for particle sizes smaller than 14 nm.[50,51]

SAED images (Fig. 3(d–f)) reveal a polycrystal-type electron diffraction pattern with an interplanar distance of 0.35 nm which corresponds to the (101) plane of the anatase phase.[52,53] The TiO_2 NP morphology suggests that as-formed TiO_2 clusters are constructed of primary building particles with different orientations. The SAED from one of these zones confirms the

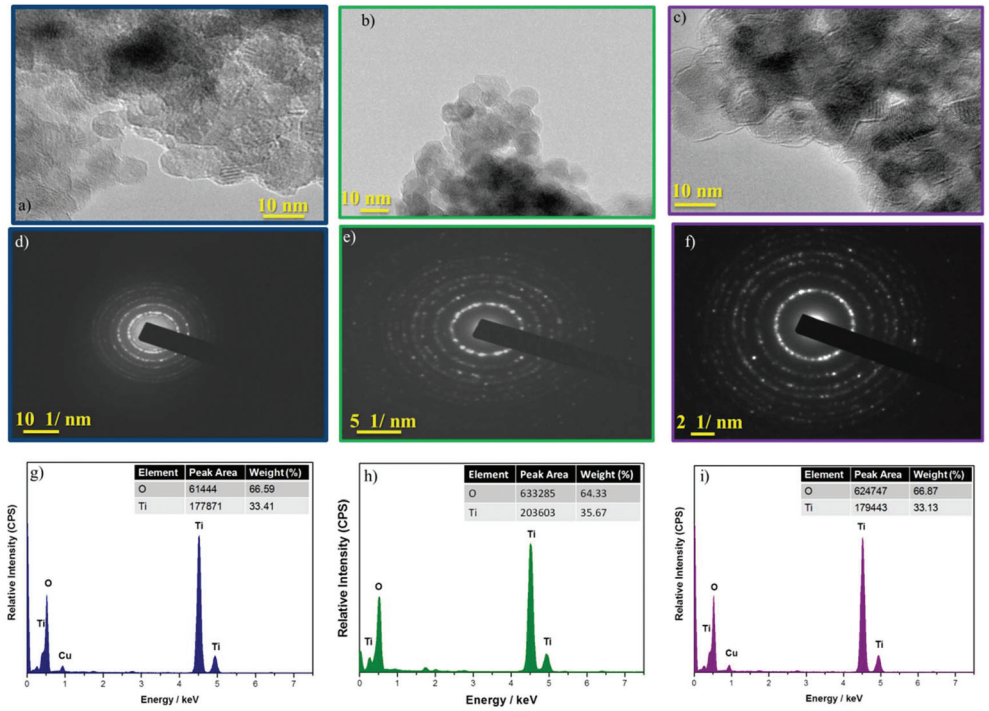

Fig. 3 HR-TEM image, EDX spectra and SAED patterns of the TiO_2 nanoparticles processed in 2 minutes (a, d, g), 8 minutes (b, e, h) and 32 minutes (c, f, i) by the microwave-assisted solvothermal method at 120 °C.

presence of high crystallinity in both anatase and brookite phases, which is in good agreement with XRD results.

The EDX is considered a qualitative or semi-quantitative technique able to provide information about elemental composition and thus obtain the stoichiometry of the material, with detection limits of 0.1 wt%, depending on the atomic number of the atom constituents.[54]

Usually TiO_2 is a compound that presents an oxygen deficiency on the lattice and commonly is represented as a nonstoichiometric compound through the formula TiO_{2-x}, where x is the effective deviation from stoichiometry (TiO_2).[55,56a] Point defects in the crystal lattice may be created in the reduced or oxidized TiO_2 forms within a simple phase regime. In the reduced form, donor-type defects such as oxygen vacancies and titanium interstitials might be created, giving features of an n-type semiconductor, the behavior of a p-type semiconductor is expected under prolonged oxidation of the TiO_2, due to the presence of point defects assigned to titanium vacancies.[56a,b] Therefore, the more appropriate way of representing the chemical formula of titanium dioxide, admitting deficits in both oxygen and cation sublattices, is through the formula $Ti_{1+x}O_{2-y}$, where Ti_{1-x} represents the titanium interstitials or titanium vacancies, while O_{2-y} is ascribed to oxygen vacancies.[56b] However, the formula TiO_{2-x} is well accepted to represent the nonstoichiometry found in TiO_2 NPs, once the titanium interstitials are minority defects present in the bulk, subsurface or surface and are generated rather at elevated temperatures, *i.e.*, by increasing the annealing temperature.[56c,d]

The stoichiometric composition from the O : Ti ratio of the TiO_2 NPs was further confirmed by EDX (see Fig. 3(g–i)) analysis and the values obtained were 1.99, 1.80 and 2.01 for the TiO_2 NPs processed in 2, 8 and 32 minutes, respectively. As can be observed by oxygen and titanium wt% results from EDX spectra, the TiO_2 NPs are nonstoichiometric compounds for samples processed at 2 and 8 minutes, while the O : Ti ratio for TiO_2 NPs processed at 32 minutes seems to be most close to TiO_2 stoichiometry. Therefore, the nonstoichiometry observed by EDX results does not actually show a systematic variation of elemental composition as a function of processing time.

The crystal growth process includes the nucleation and growth of particles. The particle size depends on the nucleation rate where a higher nucleation rate results in a smaller particle size.[57] Crystal growth by aggregation can occur by many mechanisms, including interactions of randomly oriented particles (*i.e.*, coalescence) or highly oriented particles (*i.e.*, oriented attachment).[58,59] Our results indicate that the formation of these aggregates does not proceed *via* the classical ion-attachment mechanism, but by oriented aggregation of small primary subunits. As a consequence, this mechanism involves the formation of a high concentration of aggregated nanoparticles with the predominant growth controlled by the coalescence process.[60]

In concentrated hydrochloric acid solutions, chloride ions, Cl^-, can be coordinated to the Ti^{+4}, but the complexes are not very stable;[61] consequently, chloride does not seem to have a

specific role in titania crystallization. The influence of the Cl^- ions was investigated by Jolivet and co-workers.[60] They reported that Cl^- ions seem to be essential for brookite phase formation. Our results are in very good agreement with results obtained in other experimental studies.[62,63]

Another important factor associated with acidic media is related to the mechanism of acidic catalysis in the condensation reaction for TiO_2 network formation in the sol–gel process. In this mechanism, titanium alkoxide is quickly protonated and on decreasing the electron density of the metal atom (Ti^{+4}) it becomes more electrophilic and more susceptible towards water attack and results in the formation of a penta-coordinated [TiO_5] transition state through an S_N2 mechanism.[20,21] Thus, in the MAS method, the crystal structure as well as the formation of anatase and brookite phases of the TiO_2 NPs in very acidic media seems to be controlled by the nature of the anions in the medium during processing. A similar argument was employed by Kalathil and co-workers[63] to justify that the formation of anatase and brookite TiO_2 with various morphologies can be tailored using various acid concentrations. More recently, Moura and co-workers[64] obtained TiO_2 in the presence of the anatase and brookite phases by a similar solvothermal route; however the microwave time processing employed (1 to 60 minutes) promoted changes in the morphology (spheres and sticks) with micrometer size.

Optical properties and XPS analysis

The Kubelka–Munk method[38] was employed to calculate the optical band gap energy and is described in detail in the ESI.† The UV-vis spectra in Fig. 4 show the variation in the E_{gap} values from 2.71 to 2.98 eV (2, 8 and 32 min of heat treatment process times), which are lower than those for anatase (3.20 eV).[65a,b] These values depend mainly on preparation methods and experimental conditions such as precursor purity, processing time, *etc*. These key factors can advance or inhibit the formation of structural defects which are able to control the degree of structural order and disorder of the material and, consequently, the number of intermediary energy levels within the band gap[66] or due to a quantum effect.[67]

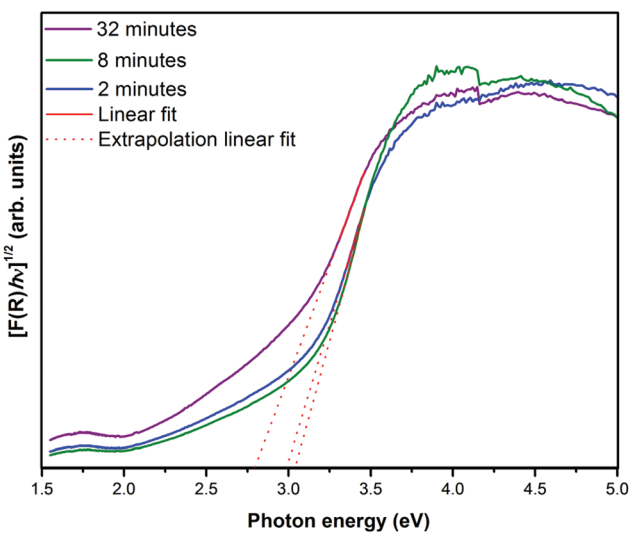

Fig. 4 UV-vis spectra of the powder TiO_2 nanoparticles processed by the microwave-assisted solvothermal method at 120 °C in 2, 8 and 32 minutes.

We believe that the decrease in the band gap value can be attributed to structural defects and local bond distortions according to results shown in Table 1 (variation in the atomic coordinates of the Ti and O atoms) and is also due to the occurrence of a second phase assigned to brookite, as well as surface defects which are able to generate states with localized electronic levels within the forbidden band gap. Due to microwave effects under solvothermal conditions, parts of the material can crystallize, dissolve and recrystallize several times.[22,68] This recrystallization process might lead to both surface and bulk modifications that change the structural order which is directly linked to the rise of new energy levels in the band gap.

XPS is a powerful technique used to explore and characterize the presence of defects in bulk (<0.5 nm), thin films, surfaces, and interfaces in electronic structure studies. Besides the aim of studying the surface chemical composition and the oxidation states of the TiO_2 NPs, XPS was employed to investigate the presence of possible defects and the electronic structure by an evaluation of the valence band (VB) in the low energy range of the survey XPS spectrum (see Fig. 5).

The XPS survey spectra of the TiO_2 nanoparticles processed for 2, 8 and 32 minutes by the MAS method are shown in Fig. 5(a). The peaks observed at above 900 eV correspond to Auger lines from O_2 (O KLL), Ti (Ti LMM) and C (C KLL). Despite the presence of carbon (assigned to the Auger line (C KLL) and the C 1s orbital), employed for the sample charging, no impurity related peak could be observed. All the values related to XPS survey spectra are shown in more detail in Table S2 (see ESI†). Fig. 5(b) shows the high resolution spectra of the O 1s core level spectra de-convoluted into three symmetric peaks using an asymmetric Gaussian–Lorentzian function fit. The profile of the O 1s XPS spectra, for all samples, consists of a main peak at 530.06 eV that corresponds to the crystal oxygen lattice in O^{2-} bound to Ti^{4+}; minor peaks at 531.42 and 532.34 eV are assigned to oxygen vacancies[69] and surface hydroxyl groups.[70a,b] FWHM (full width at half maximum) and % area values of the de-convoluted peaks with respect to Ti 2p and O 1s XPS signals are displayed in Table S3 (see ESI†). Fig. 5(c) shows the Ti 2p XPS spectra composed of two peaks assigned to signals Ti $2p_{3/2}$ and Ti $2p_{1/2}$ localized at 458.77 and 464.51 eV, respectively, with a peak separation average of 5.75 eV assignable to Ti^{4+} ions in TiO_2.[71a–d] In the typical XPS spectra profile, the binding energy of Ti 2p XPS signals, for stoichiometric TiO_2, are not broad and there are no shoulder peaks.[72] However, sub-oxides (TiO_2, Ti_2O_3, Ti_5O_3, TiO Ti_2O, Ti_3O) may be present with different oxidation states (Ti^{2+}, Ti^{3+} and Ti^{4+}) depending on the stoichiometry.[73a–c] The sub-oxide species are comparatively lower in concentration compared to the normal oxidation state Ti^{4+}. Through appro-

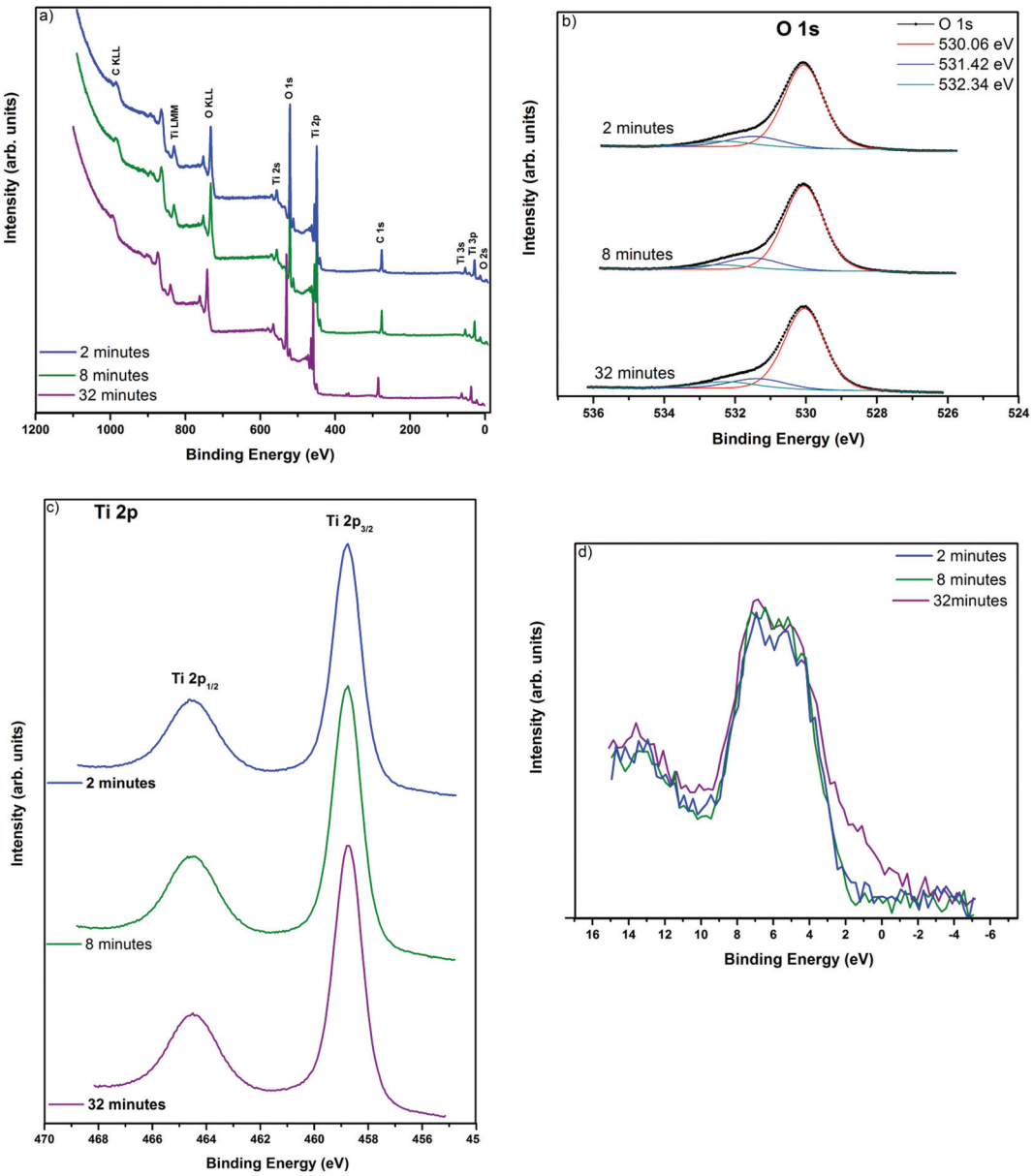

Fig. 5 (a) XPS survey spectra of the TiO_2 NPs processed in 2, 8 and 32 minutes by the microwave-assisted solvothermal method at 120 °C. (b) XPS of the O 1s region. The component at 530.06 eV is a typical signal of oxygen lattice in O^{2-} bound to Ti^4 in TiO_2 form. The O 1s XPS signal also contains two additional components which might be identified as the hydration of the surface oxide by hydroxyl groups at 532.34 eV while the peak at 531.42 eV is assigned to oxygen vacancies. (c) XPS of the Ti 2p region TiO_2 NPs. No broad profile indicates only the presence of two peaks assigned to signals Ti $2p_{3/2}$ and Ti $2p_{1/2}$ localized at 458.77 and 464.51 eV. (d) Valence band spectra obtained by enlargement of XPS survey spectra at low energy.

priate Gaussian–Lorentzian fitting, the Ti 2p XPS spectra can be used to obtain information about the oxidation states of the sub-oxides containing Ti^{3+}, Ti^{2+}, Ti^{+} and Ti^{0} ions on the surface of reduced TiO_2.[72] Fig. 5(c) illustrates the shape and position (values noted in the ESI†) of the Ti $2p_{3/2}$ XPS signals, which are independent of the processing time; the absence of broad and shoulder peaks makes it reasonable to conclude that only Ti^{4+} species are bound to O^{2-} in the TiO_2 lattice[73b] on the surface TiO_2 NPs, once Ti^{3+} surface defects and Ti^{2+} shown by Ti $2p_{3/2}$ peaks located at 457.7 and 454.4 eV, respectively, are absent.[73b–d] The O 1s and Ti 2p area (Table S2, ESI†) for these TiO_2 NPs can be used to determine the O : Ti ratio (as determined by XPS peak areas) and thus establish the stoichiometry. The results in Table S2† show that the O : Ti ratios for TiO_2 NPs processed in 2, 8 and 32 minutes were 2.48, 2.47 and 2.55, respectively, not as expected for TiO_2. However, considerations can be made regarding the O 1s XPS signals for a more realistic interpretation. Regonini and co-workers[74] determined the value of approximately 3 for the oxygen to titanium ratio (O : Ti) of the oxide films, for which contributions of the O 1s

XPS signals localized at 531.4 and 533.1 eV were ascribed to hydroxyl groups (probably some organic contaminants) and oxygen from isopropanol bonding with the outer oxide layer, respectively. Therefore, neglecting the contribution due to oxygen from water/hydrated species and from organic origins, the O : Ti ratio decreases to approximately 2.4 suggesting that the oxide films are not purely TiO_2, but rather hydrated TiO_2. In our work, also neglecting the contribution of the components from O 1s XPS signals assigned to oxygen vacancies (531.42 eV) and hydroxyl groups (532.34 eV), the O : Ti ratio decreases to approximately 2.26, 2.21 and 2.21 for TiO_2 NPs processed in 2, 8 and 32 minutes, respectively. It seems reasonable to make this approximation once 79% of the O 1s XPS signals are related to O^{2-} bound to Ti^{4+} in TiO_2 form (see Table S2, ESI†).

The values obtained by EDX TEM for the stoichiometric composition (see Fig. 3(b, d, f)) were 1.99, 1.80 and 2.01 for TiO_2 NPs processed in 2, 8 and 32 minutes, respectively, whereas XPS analyses obtained 2.26, 2.21 and 2.21 for the same samples. Thus, like the O : Ti ratio observed by EDX results, also those from XPS results are not able to show a systematic variation of elemental composition as a function of processing time. These deviations observed might be related to the qualitative nature of the EDX technique and to the fact that EDX is more representative of the bulk than of the surface,[54] whereas XPS is a technique most sensitive to surface chemical analysis which can detect the composition of samples, in atomic content (at%), up to 10 nm in thickness.[75] Hence, the absorbed species such as hydroxyl groups and probably some organic contaminants might be strongly bound to TiO_2 NPs. Since the physically absorbed species on the TiO_2 surface can be easily eliminated by XPS conditions under a ultrahigh vacuum system, a purely TiO_2 single crystal or TiO_2 with a fine surface structure will not show XPS signals.[76,77] However, the complexity of bound hydroxyls excludes XPS analysis as a suitable technique for providing a more detailed analysis of the surface hydroxyl groups bound to the TiO_2 surface.

Therefore, as XPS analysis of the Ti 2p peaks did not detect the presence of Ti^{3+}, which is assigned to surface defects in TiO_2, we believe that TiO_2 NPs contain a disorder at the interface such as surface and/or grain boundaries, due to the fact that nanosized TiO_2 materials exhibit a large interface-to-volume ratio.[69,78] For anatase, generally the surface states are oxygen vacancies or Ti^{4+} ions adjacent to oxygen vacancies.[79a,b] The rise of the oxygen vacancies will be discussed later in detail.

A brief and qualitative evaluation of the VB spectra, shown in Fig. 4(d), can be a helpful tool to assist in understanding the rise of the defect state. This fact plays an important role in better understanding the optical behavior for these TiO_2 NPs. As is well-known, pure anatase TiO_2 has primarily a filled VB derived mainly from O 2p ($2p_x$, $2p_y$ and $2p_z$) orbitals separated from an empty conduction band (CB) derived from Ti 3d orbitals ($3d_{x^2-y^2}$, $3d_{z^2}$, $3d_{yz}$, $3d_{zx}$ and $3d_{xy}$) by a bulk band gap of 3.2 eV.[65a,b] Sm^{3+} doped TiO_2 [80] with anatase and rutile crystal structures showed a different electronic structure, where impurity energy levels were created from Sm-4f states hybridized with the O 2p states above the VB and other Sm-related energy levels located in the energy range of −3 to 0 eV, for the anatase crystal structure. The Sm^{3+}-doped TiO_2 for rutile, Sm-related impurity energy levels are localized at the CB in the energy range of 4–6 eV. Therefore, the structural order assigned to the crystal structure (anatase and rutile) determined the behavior of the electronic structure associated with Sm^{3+}-doping. The VB displays (Fig. 5(c)) show the same behavior of the electronic structure for the TiO_2 NPs processed for 2 and 8 minutes, in which the electronic structure is close to the Fermi edge. However, the presence of the shoulder close to the Fermi edge is most evident for TiO_2 NPs processed for 32 minutes. The shift of the Fermi level arises from the defect state found at the top of the VB, as observed by a decrease in the optical band gap energy which is in good agreement with UV-vis results.

In terms of the optical properties, the E_g involves the surface and bulk contributions which are assignable to the arrangement of the energy levels within the band gap.[81a–c] Although the properties that arise from the creation of intermediary energy levels within the band gap are commonly found in doped semiconductor materials, undoped materials processed by a specific synthetic method may present these properties due to a degree of structural disorder at short, medium or long range.[82a]

We believe that TiO_2 NPs processed for 32 minutes undergo more recrystallization steps under hydrothermal conditions *via* microwave heat than TiO_2 NPs processed in 2 and 8 minutes, leading to a larger structural disorder capable of creating a slightly larger concentration defect that promotes the arrangement of the intermediary energy levels within the band gap. Since the factors such as the preparation method, particle morphology, heat treatment temperature, and processing time are factors that promote changes in the different structural defects such as formation of oxygen vacancies, modifications of the bond lengths, changes in the dihedral angles and distortions on the clusters which may give rise to intermediary energy levels within the band gap.[82b]

Therefore, the Fermi level is shifted (Fig. 4(d)) by the arrangement of the intermediary energy levels at the top of the VB associate to degree of structural order–disorder at long-range due to symmetry breaking, assigned to presence of the brookite phase (shown by XRD and Rietveld refinement), whereas at short-range from MR results it appears that the TiO_2 NP structure is more ordered.

UV–vis spectroscopy is a technique that can be combined with PL spectroscopy to understand the density of structural defects which are able to generate intermediary energy levels within the band gap and control the degree of structural order–disorder in the lattice.[82a] PL spectroscopy is very useful to obtain information about the electronic, optical and photoelectric properties of materials.[83,84]

PL studies might provide information on the structure, defects and impurities in a material.[82a–c,d] PL properties are a powerful probe for investigating changes around the site environment at short-range (2–5 Å) and medium-range order

(5–20 Å) of clusters where the degree of local order is pronounced.[66,82a,c] Structurally inequitable sites can be distinguished because of their different types of electronic transitions that are linked to a specific structural arrangement.[65a,82a–c] In this context, we can understand the nanostructural problem as pointed out by Billinge and Levin[85] about existing problems in determining the atomic structure of nanomaterials: "we don't have robust broadly applicable quantitative methods for solving structures at the nanoscale, and this is precisely the domain where the crystallographic methods lose their power".

PL measurements demonstrate energy transfer processes where specific structural rearrangements occur. PL emissions can be related to several factors that change electron transitions in the band gap; *i.e.* by defects related to stresses and strains on the lattice (tilts),[86a] cation or anion vacancies,[86b,c] surface states,[86d] and quantum confinement.[67] Defects that produce deep levels generate intermediary energy levels near the CB that are represented by PL emission at low energy (yellow/red),[86b,c] while shallow levels generate states next to the VB that exhibit PL emission in regions of high energy (violet/blue).[86a]

Fig. 6(a) illustrates PL spectra of TiO_2 NPs at room temperature and under an air atmosphere. The PL spectrum covers visible electromagnetic signals in the range of 400 to 800 nm; these spectra are broad and are typical of a multiphonon process; *i.e.*, a system where relaxation occurs by several paths involving the participation of numerous states within the band gap of the material.[82a,86d]

Therefore, the PL emissions cannot be ascribed to the direct recombination process between a conduction band electron in the Ti 3d orbital and a hole in the O 2p valence band. The wide band profile of the observed PL behavior is associated with several radiative and/or non-radiative luminescent centers generated from defect density. The structural disorder in the crystal lattice promotes a polarization effect due to redistribution of electron density by changes in the bond lengths and bond angles between Ti and O atoms resulting in the non-uniform electronic structure.

An analysis of PL spectra (see Fig. 6(a)) shows that TiO_2 NPs have a maximum emission associated with PL emissions at 539 nm, 534 nm and 528 nm, for 2, 8 and 32 minutes of processing time, respectively. Therefore, the PL emission bands are slightly displaced as a function of processing time. The wide PL band emissions show a blue shift between PL emission bands for 2 and 8 minutes and a red shift between PL emission bands for 8 and 32 minutes. The PL shifts seem to indicate that the concentration and the nature of the defects created in TiO_2 NPs depend on the degree of structural order–disorder, which is intimately related to the processing time of heat treatment.

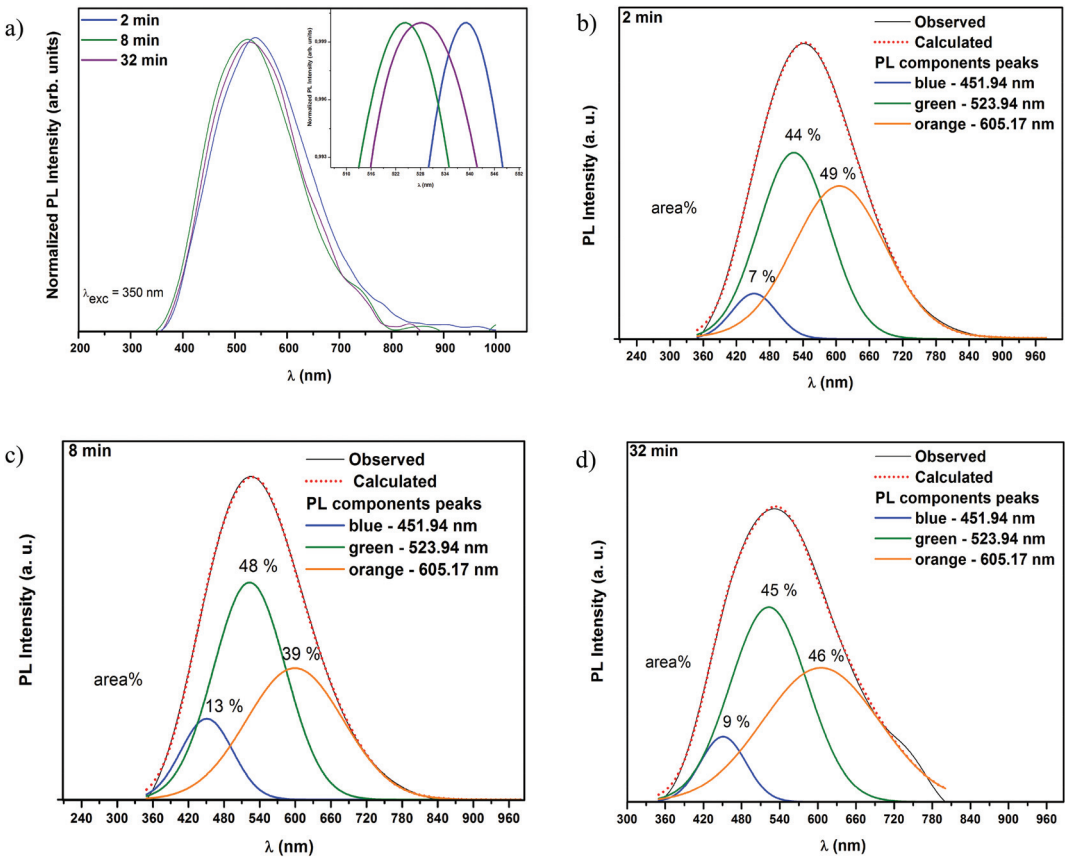

Fig. 6 (a) Normalized PL spectra at room temperature under an air atmosphere of the TiO_2 NPs (powder) and insert of displacements of PL emission bands. Deconvolution of the PL spectra for (b) 2 minutes, (c) 8 minutes and (d) 32 minutes.

It appears reasonable to correlate the PL energies to intermediary energy levels within the band gap,[69] once the PL emissions localized at 539 nm (≈2.30 eV), 534 nm (≈2.30 eV) and (≈2.35 eV) (see Fig. 6a) are lower than the experimental optical band gap energy (see Fig. 4).

To gain a deeper insight regarding the emissions, the PL spectrum was deconvoluted with a Voigt function using the PeakFit program (4.05 version).[87] The PL spectra can be deconvoluted into three peaks (PL sub-bands), which are centered at 451, 523 and 605 nm, and are ascribed to components in the blue, green and orange regions, respectively. Each component contributes to the wide band profile and is linked to a specific structural defect. The analysis of the deconvoluted peaks (see Fig. 6(b–d)) confirms that the variation in the emission intensity (% area) of the components (blue, green and orange) can be explained by the variation in the defect density created during the processing time employed in the MAS method.

PL behavior for TiO_2 anatase is associated with three kinds of physical origins: self-trapped excitons (STEs),[88] oxygen vacancies,[89] and surface states.[90] The PL band localized in the ultra-violet (violet/blue) region is characteristic of an intrinsic luminescence, *i.e.* structural defects, that causes distortions on the coordination polyhedron hexa-coordinated [TiO_6] clusters of the anatase,[86a,88] whereas extrinsic luminescence emissions are situated at low energy (green/yellow) and are associated with oxygen vacancies and surface states.[86b–d]

According to the literature[82b] the factors related to the preparation method can promote a degree of structural disorder capable of giving rise to different structural defects. The internal/external vibration between adjacent strongly bound clusters provide information about the degree of structural order–disorder in the lattice.[82c,90] Nonetheless, the symmetry breaking of these clusters leads to distortions on the clusters, modifications in the O–Ti–O bond lengths, changes in the dihedral angles and formation of oxygen vacancies.[90,91] Hence we believe that the degree of structural disorder related to symmetry breaking due to the brookite phase as well as heat treatment from the MAS method might be responsible for distortions (tilts) on the [TiO_6], changes in the O–Ti–O bond lengths and formation of oxygen vacancies, which latter could act as donors for charge carriers, trap sites of electrons, and/or recombination centers.[69]

It is well-established that the relationship between the degree of structural order–disorder in the bulk and the surface[81a–c] contributes to the wide band profile[82a–c] observed, which can be distinguished by the degree of perturbation contained on the TiO_2 NP lattice at short, medium or long-range.

Bond lengths and bond angles between titanium and oxygen atoms from the atomic coordinates obtained by Rietveld refinement results are displayed in Table S4 (see ESI†). The bond length and bond angle values were calculated using Visualization for Electronic and Structural Analysis (version 3 for Windows),[92] and the unit cell parameters of ICDS CIF no. 24276 and CIF no. 31122 were used as the reference.[36,37] The results show that [TiO_6] clusters, both anatase and brookite, are slightly distorted on the cell unit by the variation in the bond lengths (Ti–O_n (n = 1, ..., 6)) and the bond angles, formed between two oxygen atoms and the titanium atom (ψ,ϕ, φ, ε, γ andδ), on the TiO_2 NP lattice. As the crystallization process proceeds during the processing time, the several crystallization steps under hydrothermal conditions aided by the fast heat of the MAS method promote a structural arrangement for each crystallization step by shifting the atomic coordinates of the oxygen and titanium atoms, thus obtaining a network formed by distorted clusters that leads to a symmetry breaking, resulting in an asymmetric charge distribution[82a–c] in the intermediate-range order, which confirms additional electronic levels within the band gap. By comparing the results obtained by the Rietveld refinement (see Table 1), and the deviations in the bond lengths and bond angles compared to theoretical values and the deconvolution of the PL spectra (see Fig. 6(b–d)), it is reasonable to conclude that there is a degree of structural disorder due to symmetry breaking[82c,90] linked to oxygen vacancies, with different charged states ($V_O^{\bullet}$ and $V_O^{\bullet\bullet}$) or in a neutral state (V_O^{x}),[93] that acts on the arrangement of the energy levels within the band gap region leading to changes in the electron density in the TiO_2 NP crystal lattice, where each PL sub-band (blue, green and orange) is related to one kind of electronic transition between the several energy levels created within the band gap.

The order–disorder of the TiO_2 and titanate structures can lead to an ordered structure with [TiO_6] cluster makers, and another disordered structure which is ascribed to a [TiO_6] slightly distorted cluster and another [TiO_5] complex cluster, which all are related to a specific type of oxygen vacancy.[91,93] Hence, two effects which are attributable to TiO_2 NP PL behavior can be identified from the degree of structural order–disorder due to defects ascribed to oxygen vacancies on the TiO_2 NP network. The first effect emerges from the deformations (tilts) induced in the [TiO_6] octahedral clusters and deviations in the bond lengths that promote a slight shift in the oxygen atom position that gives rise to intermediary energy levels within the band gap, which are responsible for the luminescent centers at high energy (blue component).[86a,88] The second effect is derived from a slightly larger displacement in the oxygen atom position that might be understood as a defect near the surface, not assigned to the presence of Ti^{3+} sites but those, *i.e.* due to surface dangling bonds,[69] resulting in another type of oxygen vacancy on the TiO_2 NP lattice which are represented by [TiO_5] complex clusters. This second effect also promotes narrowing of the optical band gap energy by generating intermediary energy levels within the band gap, which are responsible for the low energy luminescent centers (green and orange components).[86b,c] The mechanism shown in Fig. 7 explains the PL behavior at room temperature of TiO_2 NPs processed by the MAS method for different processing times.

Bulk, surface and interface defects may be possible trap sites for charge carriers.[81a–c,82a] Temperature-variable PL of the highly crystalline TiO_2 nanotube, as a function of wall thicknesses of ~20 nm, show that at low temperature (<50 K) electrons would occupy the trap sites without thermal excitation, and hence STEs become predominant in the direct relaxation,

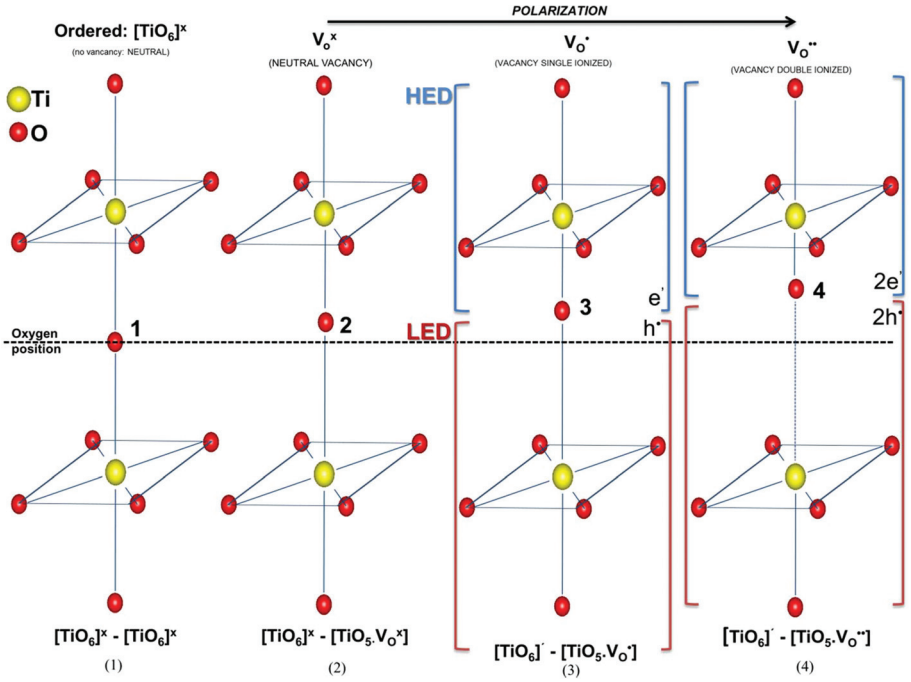

Fig. 7 Scheme of the polarization effect under the TiO_2 NP lattice due to oxygen vacancies (V_O^x, $V_O^{\bullet}$ or $V_O^{\bullet\bullet}$). The relationship between structural order–disorder is ruled by the dynamics of transformation from ordered $[TiO_6]^x$ clusters to distorted $[TiO_6]'$ and complex $[TiO_5{\cdot}V_O^x]$, $[TiO_5{\cdot}V_O^{\bullet}]$, $[TiO_5{\cdot}V_O^{\bullet\bullet}]$ clusters.

while at high temperature (>50 K) due to the thermal quenching by non-radiative recombination, STEs are suppressed by oxygen vacancy states.[69]

Therefore, disorder generates imbalanced charges on the structure and leads to formation of electrons and holes in the TiO_2 NP lattice. During the excitation process in the crystals, the electronic transitions involve more than one kind of cluster on the lattice where the charge transfer takes place between clusters,[81b,c] whereas in the relaxation process the recombination of excitons might be trapped by energetic states within the band gap[82a] or might be trapped/detrapped in sites into $[TiO_6]$ clusters generated from local distortions on the lattice assigned to a specific phonon mode.[69,94] However, the increase of temperature promotes the decrease or extinction of the defects assigned to structural local disorder in the lattice.

The assumption is made that one oxygen vacancy is not necessarily linked to an insufficiency of oxygen atoms on the TiO_2 crystal lattice but rather a displacement in the oxygen atomic position leading to a polarization effect. The bond lengths (Ti–O) increase, which is the charge transport in the crystal lattice. Fig. 7 shows a scheme of oxygen vacancy types that might be present in the TiO_2 NP lattice.

The picture shows only two $[TiO_6]$ adjacent clusters, but the model extends to the surface and all bulk NPs. In (1), the $[TiO_6]$ clusters show the oxygen atom position representing the most structurally ordered arrangement of the TiO_2 crystal lattice without oxygen vacancies. It is assumed that the no vacancy condition refers to the structural arrangement using the bond lengths (Ti–O) and bond angles (O–Ti–O) of the theoretical values of the anatase (ICDS no. 24276) and brookite (ICDS no. 31122) phases. In (2) the oxygen atom, between two adjacent clusters, refers to a structural arrangement which is assigned to neutral oxygen vacancy (V_O^x) that representing a structure slightly disordered, where the oxygen atom position is slightly displaced compared to the theoretical structural arrangement position 1. Therefore, a slight polarization[91] begins to emerge. In (3), increases in the bond lengths (O–Ti) or distortions (tilts) on the $[TiO_6]$ octahedral cluster begin to redistribute the charges in the crystal, resulting in two regions with slightly different electronic densities. The electron will be closer to the $[TiO_6]$ cluster where the distortion is larger or the cluster where the oxygen atom will be closest to forming the single ionized ($V_O^{\bullet}$) oxygen vacancy. When the distortions or bond lengths increase to a still larger displacement (4) of the oxygen atom, a polarization effect, due to the larger charge separation, might occur creating a high electronic density region (HED) and another with a low electronic density region (LED). For this effective polarization effect the oxygen vacancy double ionized ($V_O^{\bullet\bullet}$) is associated. In positions 2, 3 and 4, the increase of the displacement of the bond length (Ti–O) followed by one sharp distortion on the $[TiO_6]$ octahedron gives rise to complex $[TiO_5]$ clusters, represented by $[TiO_5{\cdot}V_O^x]$, $[TiO_5{\cdot}V_O^{\bullet}]$ and $[TiO_5{\cdot}V_O^{\bullet\bullet}]$ species respectively, unlike in picture 1, in which the network is formed only by $[TiO_6]^x$ clusters. Therefore, instead of the idea of insufficient oxygen atoms,[95] the oxygen vacancies V_O^x, $V_O^{\bullet}$ and $V_O^{\bullet\bullet}$ on the TiO_2 NPs can be understood by bond length displacement (Ti–O) capable of promoting distortions on the TiO_6 octahedral clusters as well as modifications in the bond lengths, bond angles or dihedral angles, and are associated with $[TiO_6]^x$ clusters, which

represent the most ordered TiO_2 structure, according to the following equations:

$$[TiO_6]^x + [TiO_5{\cdot}V_O{}^x] \rightarrow [TiO_6]' + [TiO_5{\cdot}V_O{}^{\bullet}] \quad (1)$$

$$[TiO_6]^x + [TiO_5{\cdot}V_O{}^{\bullet}] \rightarrow [TiO_6]' + [TiO_5{\cdot}V_O{}^{\bullet\bullet}] \quad (2)$$

$$[TiO_6]^x - [TiO_6]^x \text{ (position 1)} \quad (3)$$

$$[TiO_6]^x - [TiO_5{\cdot}V_O{}^x] \text{ (position 2)} \quad (4)$$

$$[TiO_6]' - [TiO_5{\cdot}V_O{}^{\bullet}] \text{ (position 3)} \quad (5)$$

$$[TiO_6]' - [TiO_5{\cdot}V_O{}^{\bullet\bullet}] \text{ (position 4)} \quad (6)$$

Eqn (1) and (2) show the transformation of the TiO_2 highly ordered structural neutral network, formed by $[TiO_6]^x$–$[TiO_6]^x$ clusters, to a slightly polarized network formed by $[TiO_6]'$–$[TiO_5]$ due to structural disorder arising from oxygen vacancies $V_O{}^x$, $V_O{}^{\bullet}$ and $V_O{}^{\bullet\bullet}$. The $[TiO_6]'$ clusters, unlike $[TiO_6]^x$, are a distorted octahedron that give rise to a slight polarization effect in the TiO_2 NP crystal lattice when the oxygen atom displacement becomes larger as compared to position 1, and/or as soon as the tilts increase. The relationship between defects and PL observations can be understood by noting the concentration of the maker species of the TiO_2 NP network, *i.e.* $[TiO_6]^x$, $[TiO_5{\cdot}V_O{}^x]$, $[TiO_6]'$, $[TiO_5{\cdot}V_O{}^{\bullet}]$, and $[TiO_5{\cdot}V_O{}^{\bullet\bullet}]$. The concentration of these species is based on the dynamics of the transformation of the $[TiO_6]$ clusters, represented by $[TiO_6]^x$ and $[TiO_6]'$ to complex $[TiO_5]$ clusters, represented by $[TiO_5{\cdot}V_O{}^x]$, $[TiO_5{\cdot}V_O{}^{\bullet}]$ and $[TiO_5{\cdot}V_O{}^{\bullet\bullet}]$.

Therefore, the TiO_2 NP network is formed by a relationship between the structural order–disorder induced by oxygen vacancies that at long range, distorted $[TiO_6]'$ and complex $[TiO_5{\cdot}V_O{}^x]$ clusters are assigned to interface anatase/brookite phases and tilts on the $[TiO_6]$ octahedron and slight changes in the bond lengths and bond angles between oxygen and titanium atoms that give rise to shallow levels within the band gap close to CB responsible for luminescent centers at high energy, and by complex $[TiO_5{\cdot}V_O{}^{\bullet}]$ and $[TiO_5{\cdot}V_O{}^{\bullet\bullet}]$ clusters which might be understood as dangling bonds defects near the surface, giving rise to deep levels within the band gap close to VB responsible for PL emissions at low energy. Both shallow and deep levels might act as acceptors/donors for charge carriers, trap sites of electrons, and/or recombination centers. While at short-range the TiO_2 NP structure is more ordered, the increase of the processing time does not promote local distortions capable of changing the periodic spacing in the $[TiO_6]$ octahedra, due to the presence of only phonon Raman active-modes assigned to vibrations intrinsic to the anatase lattice for all TiO_2 NPs. On the other hand, the TiO_2 NP lattice is formed by a network from interactions between different cluster makers (as shown in Fig. 8), so it seems reasonable to conclude that at medium-range there is a slight

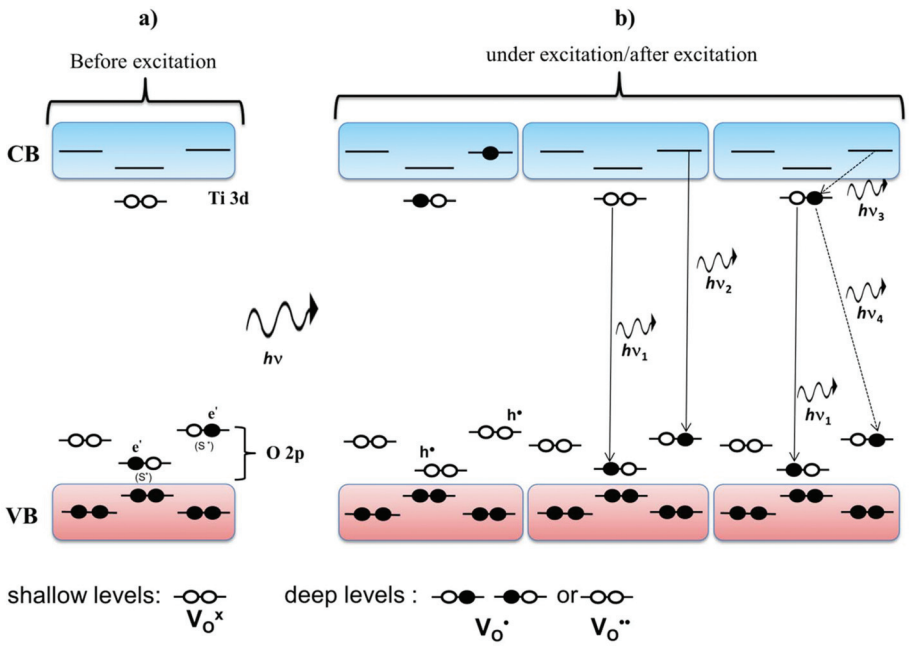

Fig. 8 Scheme of the PL wide band model proposed. Before the excitation process (a): the electrons at the VB might occupy the energy levels (deep levels) most close to the VB created by structural disorder giving rise to the ground state (S*). Under excitation/after excitation (b): after excitation (laser λ = 354 nm), the electron–hole pair is created in which the hole (h$^{\bullet}$) is trapped at deep levels while the electron (e′) might be trapped by shallow levels close to the CB. The electrostatic attraction of these charges occurs generating an instable exciton pair that is suppressed *via* radiative decay ($h\nu_1$). As the excitation energy is larger than the band gap, electrons might be excited directly from deep levels to the CB and fall back again to deep levels *via* radiative decay $h\nu_2$ or once the CBs suffer successive relaxation processes falling back again to low energy states (to both shallow and deep levels) *via* radiative decays ($h\nu_1$, $h\nu_2$, $h\nu_3$, $h\nu_4$,...,$h\nu_n$). Therefore, the PL wide band observed is a result of all radiative decays that happens within the band gap ($h\nu_1 + h\nu_2 + \cdots + h\nu_n$).

degree of structural disorder caused by distortions in the dihedral angles[82c,90] between adjacent clusters, once to an ordered structure the dihedral angles are related to the equilibrium position between ordered clusters $[TiO_6]^x$–$[TiO_6]^x$; however the cluster makers of the disordered structure of the TiO_2 NPs are $[TiO_6]^x$–$[TiO_5{\cdot}V_O^x]$, $[TiO_6]'$–$[TiO_5{\cdot}V_O^{\bullet}]$ and $[TiO_6]'$–$[TiO_5{\cdot}V_O^{\bullet\bullet}]$, in which the bond lengths (Ti–O) and bond angles (O– $\widehat{\text{Ti}}$ –O) are slightly distorted, hence exhibit distortions in the dihedral angles.

Oxygen vacancies on the disordered structure[82c,91,93] work as electron trapping or hole trapping centers which generate intermediary levels within the band gap according to eqn (2) and (3), where $[TiO_6]'$ is the donor, $[TiO_5{\cdot}V_O^{\bullet}]$ is the donor or acceptor, and $[TiO_5{\cdot}V_O^{\bullet\bullet}]$ is the acceptor. $[TiO_5{\cdot}V_O^x]$ is a neutral complex with two unpaired electrons; $[TiO_5{\cdot}V_O^{\bullet}]$ has one unpaired electron and $[TiO_5{\cdot}V_O^{\bullet\bullet}]$ has no unpaired electrons. These equations suggest that electrons trapped (+) in an oxygen vacancy complex are a necessary requirement for the formation of polarons during the excitation process that changes the electronic density of the crystal, causing a polarization effect.[91,93,96] Similar arguments have been used very recently to represent oxygen vacancies in the case of SnO_2 quantum dots.[97]

A wide band model (Fig. 8) was proposed based on the electronic transitions that might occur between the intermediary energy levels in order to explain the origin of the PL emissions for TiO_2 NPs. In the PL model proposed, an important step occurs before the excitation process that strengthens the argument about intermediary energy levels created within the band gap. Before the excitation process (Fig. 8a), deep levels are created close to the VB and thus the electron might occupy these levels (an excited state (S*)), changing the electronic arrangement. Therefore, when the electrons occupy these energy levels close to the VB, this electronic arrangement is defined as the ground state since no energy source (electromagnetic) acts under TiO_2 NPs, only thermal energy at room temperature. Hence, the excitation of the crystal lattice might occur *via* phonons. After being excited (Fig. 8b) by an energy source ($h\nu$), positive holes ($h^{\bullet}$) in the S* and negative electrons (e') are created in the CB or in some intermediary energy levels (shallow levels) close to CB. Thus, charge carriers and trap sites are present in the hole–electron (e'–$h^{\bullet}$) recombination pairs to explain the PL behavior of TiO_2 NPs that occur from the mechanism where:

(1) the positive holes created in the S*, after the electron is excited, can be electrostatically attracted by the electron trapped by shallow levels close to the CB, generating an exciton pair which due to their instability suffers annihilation *via* radiative decay ($h\nu_1$);

(2) once the light source excitation energy (laser λ = 354 nm) is greater than the optical band gap energy (see UV-vis results) there is a possibility that the electron localized at S* is not trapped by deep levels close to VB, but rather becomes excited toward the CB by band–band transitions which fall back again to deep levels *via* radiative decay ($h\nu_2$);

(3) at CB, the electron might undergo recombination toward shallow levels closest to the CB *via* radiative decay $h\nu_3$ and keep successive relaxation processes falling back again to adjacent deep levels *via* radiative decays $h\nu_3$, $h\nu_4$, ..., $h\nu_n$.

Therefore, the energies arising from these electronic transitions are converted in photons ($h\nu$), by several radiative decays ($h\nu_1$, $h\nu_2$, $h\nu_3$, $h\nu_4$, ..., $h\nu_n$) originated during the multiple radiative electronic transitions which are responsible by PL wide band emissions.[82a–c,90,91,93,96]

The concentration of intermediary energy levels (shallow and deep levels) within the band gap is related to the concentration of defects generated by the degree of structural order–disorder from oxygen vacancies (V_O^x, $V_O^{\bullet}$ and $V_O^{\bullet\bullet}$). According to the deconvolution of the PL spectra, the contribution of each PL sub-band (blue, green and orange) occurs in a random way, *i.e.*, is not related to the processing time of the TiO_2 NPs. However, the contribution (% area) of the PL sub-bands (green and orange) is larger than the blue component. Therefore, it seems reasonable to conclude that the PL behavior is dominated by luminescent centers responsible for PL emission at low energy. Hence, the concentration of deep levels within the band gap is larger than shallow levels, once the defects originating from structural disorder assigned to $[TiO_5{\cdot}V_O^{\bullet}]$ and $[TiO_5{\cdot}V_O^{\bullet\bullet}]$ complex clusters are responsible for PL sub-bands at low energy (green and orange). So, the concentration of these species on the TiO_2 NP lattice is larger.

Conclusions

From a quantitative analysis of the results, we have confirmed in this study a correlation between structural and electronic order–disorder effects at long, medium and short-range and their optical properties for TiO_2 nanoparticles synthesized by the sol–gel process followed by the MAS method. During the sol–gel conventional process, without any heat treatment, the formation of connections along the network of $[TiO_6]$ clusters, *via* Ti–O–Ti, is very slow. However, when the MAS method is employed, the Ti–O–Ti bond formation is promoted by a cooperative effect related to hydrolysis and condensation reactions, resulting in TiO_2 NPs with a particular structure composed by distorted lattices. The microwave assisted solvothermal process showed that only in 2 minutes it was possible to obtain TiO_2 NPs with highly oriented particles (oriented attachment).

The fast microwave heat process under hydrothermal conditions was able to promote rearrangement of the atomic coordinates of the oxygen and titanium atoms leading to symmetry breaking and additional disturbances on the bond lengths (Ti–O) and slight distortions on the maker species (clusters) which are related to oxygen vacancies (V_O^x, $V_O^{\bullet}$ and $V_O^{\bullet\bullet}$). Structural disorder at long and medium-range occurred, due to symmetry breaking by rich-brookite on the TiO_2 NP lattice and from slight distortions in dihedral angles present on the cluster makers, respectively. On the other hand, at short-range

the TiO_2 NP structure is more ordered due to the presence of only vibrational Raman active-modes assigned to anatase.

In fact, the oxygen vacancies might be understood as disturbances of the bond lengths (Ti–O) and distortions on the $[TiO_6]$ octahedron ascribed to the displacement of the oxygen atom position. Thus, as soon as the bulk becomes most disordered, by increases in the shift of the oxygen atom position, the oxygen vacancy changes from a neutral state (V_O^x) to a slightly polarized state ($V_O^{\bullet}$ and $V_O^{\bullet\bullet}$), transforming the highly ordered and neutral $[TiO_6]^x$–$[TiO_6]^x$ clusters to slightly polarized and disordered $[TiO_6]'$–$[TiO_5]$ clusters.

The distortions and deviations of both bond lengths and bond angles, between oxygen and titanium atoms on the cluster makers, increase the structural disorder which is associated with a specific type of oxygen vacancy. Each oxygen vacancy changes the concentration of the distorted and complex clusters $[TiO_6]'$, $[TiO_5{\cdot}V_O^x]$, $[TiO_5{\cdot}V_O^{\bullet}]$ and $[TiO_5{\cdot}V_O^{\bullet\bullet}]$ on the TiO_2 NP lattice. So, this degree of structural order–disorder gives rise to intermediary energy levels (shallow and deep levels) within the band gap, in which the transitions between these intermediary energy levels explain the origin of the PL emissions for this system. The wide band model proposed for PL behavior at room temperature is composed of three PL sub-bands (blue, green, and orange), once the green and orange components, assigned to $[TiO_5{\cdot}V_O^{\bullet}]$ and $[TiO_5{\cdot}V_O^{\bullet\bullet}]$ complex clusters, are dominant in the PL behavior. Therefore, the TiO_2 NP lattice contains a concentration of the cluster makers, $[TiO_5{\cdot}V_O^{\bullet}]$ and $[TiO_5{\cdot}V_O^{\bullet\bullet}]$, larger than $[TiO_6]'$ and $[TiO_5{\cdot}V_O^x]$ species.

We believe that these results will be of importance in understanding and controlling the properties of the TiO_2 nanoparticles and that the reported experimental approach may be used as a tool to better understand the complexity of the structural defects in the nanostructure system and can be relevant in addressing the open question of the degree of electron redistribution in undoped semiconducting oxides.

Acknowledgements

The authors are grateful to FAPESP 2013/07296-2, CAPES, CNPq INCTMN 573636/2008-7, Prometeo/2009/053 (Generalitat Valenciana), Ministerio de Economia y Competitividad (Spain), CTQ2012-36253-C03-02, and the Spanish–Brazilian program (PHB2009-0065-PC) for financially supporting this research and CAPES for the scholarship (to E.S.J. and F.A.L.) and the CAPES process A104/2013 to J.A. Special thanks are given to Dr P. Hammer (LEFE-IQ/UNESP) for help with the XPS analysis and to Dr D. Keyson and Dr D.P. Volanti for the development of the microwave-hydrothermal system.

References

1 A. Fujishima and K. Honda, *Nature*, 1972, **238**, 37–38.
2 D. A. Tryk, A. Fujishima and K. Honda, *Electrochim. Acta*, 2000, **45**, 2363–2376.
3 T. A. Arun, A. A. Madhavan, D. K. Chacko, G. S. Anjusree, T. G. Deepak, S. Thomas, S. V. Nair and A. S. Nair, *Dalton Trans.*, 2014, **43**, 4830–4837.
4 K. Bourikas, C. Kordulis and A. Lycourghiotis, *Chem. Rev.*, 2014, **114**, 9754–9823.
5 J. M. Pettibone, D. M. Cwiertny, M. Scherer and V. H. Grassian, *Langmuir*, 2008, **24**, 6659–6667.
6 T. C. Jagadale, S. P. Takale, R. S. Sonawane, H. M. Joshi, S. I. Patil, B. B. Kale and S. B. Ogale, *J. Phys. Chem. C*, 2008, **112**, 14595–14602.
7 G. Li, L. Li, J. Boerio-Goates and B. F. Woodfield, *J. Am. Chem. Soc.*, 2005, **127**, 8659–8666.
8 Q. Li, B. Cheng, X. Yang, R. Liu, B. Liu, J. Liu, Z. Chen, B. Zou, T. Cui and B. Liu, *J. Phys. Chem. C*, 2013, **117**, 8516–8521.
9 H. Z. Zhang and J. F. Banfield, *J. Phys. Chem. B*, 2000, **104**, 3481–3487.
10 (*a*) M. Lazzeri, A. Vittadini and A. Selloni, *Phys. Rev. B: Condens. Matter*, 2001, **63**, 155409–155418; (*b*) A. Barnard and L. A. Curtiss, *Nano Lett.*, 2005, **5**, 1291–1266; (*c*) A. S. Barnard, P. Zapol and L. A. Curtiss, *J. Chem. Theory Comput.*, 2005, **1**, 107–116; (*d*) F. De Angelis, C. Di Valentin, S. Fantacci, A. Vittadini and A. Selloni, *Chem. Rev.*, 2014, **114**(19), 9708–9753.
11 C. J. Howard, T. M. Sabine and F. Dickson, *Acta Crystallogr., Sect. B: Struct. Sci.*, 1991, **47**, 462–468.
12 X. Chen and S. S. Mao, *Chem. Rev.*, 2007, **107**, 2891–2959.
13 J. F. Banfield and D. R. Veblen, *Am. Mineral.*, 1992, **77**, 545–557.
14 M. Mattesini, J. S. de Almeida, L. Dubrovinsky, N. Dubrovinskaia, B. Johansson and R. Ahuja, *Phys. Rev. B: Condens. Matter*, 2004, **70**, 212101–212105.
15 V. Petkov, G. Holzhüter, U. Tröge, T. Gerber and B. Himmel, *J. Non-Cryst. Solids*, 1998, **231**, 17–30.
16 D. Reyes-Coronado, G. Rodrïguez-Gattorno, M. E. Espinosa-Pesqueira, C. Cab, R. de Coss and G. Oskam, *Nanotechnology*, 2008, **19**, 145605–145615.
17 M. Galynska and P. Persson, *Int. J. Quantum Chem.*, 2013, **113**, 2611–2620.
18 M. Landmann, T. Köhler, S. Köppen, E. Rauls, T. Frauenheim and W. G. Schmidt, *Phys. Rev. B: Condens. Matter*, 2012, **86**, 064201–0642021.
19 D. P. Macwan, N. Pragnesh Dave and S. Chaturvedi, *J. Mater. Sci.*, 2011, **46**, 3669–3686.
20 F. Peng, L. Cai, L. Huang, H. Yu and H. Wang, *J. Phys. Chem. Solids*, 2008, **69**, 1657–1664.
21 J. Livage and C. Sanchez, *J. Non-Cryst. Solids*, 1992, **145**, 11–19.
22 (*a*) T. N. Glasnov and C. O. Kappe, *Chem. – Eur. J.*, 2011, **17**, 11956–11968; (*b*) K. Zhang, J. Dai, Y.-H. Wang, M.-H. Zeng and M. Kurmoo, *Dalton Trans.*, 2013, **42**, 5439–5446.
23 I. Bilecka, P. Elser and M. Niederberger, *ACS Nano*, 2009, **3**, 467–477.

24 H. J. Kitchen, S. R. Vallance, J. L. Kennedy, N. Tapia-Ruiz, L. Carassiti, A. Harrison, A. G. Whittaker, T. D. Drysdale, S. W. Kingman and D. H. Gregory, *Chem. Rev.*, 2014, **114**, 1170–1206.
25 D. M. P. Mingos and D. R. Baghurst, *Chem. Soc. Rev.*, 1991, **20**, 1–47.
26 T. M. Atkins, A. Thibert, D. S. Larsen, S. Dey, N. D. Browning and S. M. Kauzlarich, *J. Am. Chem. Soc.*, 2011, **133**, 20664–20667.
27 I. Bilecka and M. Niederberger, *Nanoscale*, 2010, **2**, 1358–1374.
28 K. Manseki, Y. Kondo, T. Ban, T. Sugiura and T. Yoshida, *Dalton Trans.*, 2013, **42**, 3295–3299.
29 L. Pan, X. Liu, Z. Sun and C. Q. Sun, *J. Mater. Chem. A*, 2013, **1**, 8299–8326.
30 M. Baghbanzadeh, L. Carbone, P. D. Cozzoli and C. O. Kappe, *Angew. Chem., Int. Ed.*, 2011, **50**, 11312–11359.
31 D. Dallinger and C. O. Kappe, *Chem. Rev.*, 2007, **107**, 2563–2591.
32 Z. J. Luo, H. M. Li, H. M. Shu, K. Wang, J. X. Xia and Y. S. Yan, *Cryst. Growth Des.*, 2008, **8**, 2275–2281.
33 H. M. Rietveld, *J. Appl. Crystallogr.*, 1969, **2**, 65–71.
34 A. C. Larson and R. B. Von Dreele, Los Alamos National Laboratory Report LAUR, 1994, 86748.
35 L. W. Finger, D. E. Cox and A. P. Jephcoat, *J. Appl. Crystallogr.*, 1994, **27**, 892–900.
36 F. Schossberger, *Z. Kristallogr.*, 1942, **104**, 358–374.
37 R. Weyl, *Z. Kristallogr.*, 1959, **111**, 401–420.
38 P. Kubelka and F. Munk-Aussig, *Zeit. Für. Tech. Phys.*, 1931, **12**, 593–601.
39 D. A. Shirley, *Phys. Rev. B: Solid State*, 1972, **5**, 4709–4714.
40 R. Sharma, D. P. Bisen, U. Shukla and B. G. Sharma, *Recent Res. Sci. Tech.*, 2012, **4**, 77–79.
41 (*a*) S. R. Hall, F. H. Allen and I. D. Brown, *Acta Crystallogr., Sect. A: Found. Crystallogr.*, 1991, **47**, 655; (*b*) P. Thompson, D. Cox and J. Hastings, *J. Appl. Crystallogr.*, 1987, **20**, 79–82, 1987; (*c*) D. L. Bish and J. E. Post, *Am. Mineral.*, 1993, **78**, 932–940; (*d*) M. Ferrari and L. Lutterotti, *J. Appl. Phys.*, 1994, **76**, 7246–7255.
42 (*a*) E. Jansen, W. Schafer and G. Will, *J. Appl. Crystallogr.*, 1994, **27**, 492–496; (*b*) G. Will, *Powder diffraction: The Rietveld method and the two stage method to determine and refine crystal structures from powder diffraction data*, Springer-Verlag, Berlin, Heidelberg, 2006, pp. 44–69; (*c*) L. Lutterotti, M. Bortolotti, G. Ischia, I. Lonardelli and H. R. Wenk, *Z. Kristallogr., Suppl.*, 2007, **26**, 125–130; (*d*) H. R. Wenk, L. Lutterotti and S. C. Vogel, *Powder Diffr.*, 2010, **25**, 283–296; (*e*) Y. Hu, H.-L. Tsai and C.-L. Huang, *J. Eur. Ceram. Soc.*, 2003, **23**, 691–696.
43 P. Tengvall, T. P. Vikingfe, I. Lundstrom and B. Liedberge, *J. Colloid Interface Sci.*, 1993, **160**, 10–15.
44 S. Sahoo, A. K. Arora and V. Sridharan, *J. Phys. Chem. C*, 2009, **113**, 16927–16933.
45 Y. Lei, L. D. Zhang and J. C. Fan, *Chem. Phys. Lett.*, 2001, **338**, 231–236.
46 W. Hu, L. Li, G. Li, C. Tang and L. Sun, *Cryst. Growth Des.*, 2009, **9**, 3676–3682.
47 A. Golubović, M. Šćepanović, A. Kremenović, S. Aškrabić, V. Berec, Z. Dohčević Mitrović and Z. V. Popović, *J. Sol-Gel Sci. Technol.*, 2008, **49**, 311–319.
48 M. Sćepanović, M. Grujić-Brojčin, K. Vojisavljević, S. Bernik and T. Srećković, *J. Raman Spectrosc.*, 2012, **41**, 914–921.
49 V. Swamy, A. Kuznetsov, L. S. Dubrovinsky, R. A. Caruso, D. G. Shchukin and B. C. Muddle, *Phys. Rev. B: Condens. Matter*, 2005, **71**, 184302–184312.
50 H. Zhang and J. F. Banfield, *J. Mater. Chem.*, 1998, **8**, 2073–2076.
51 J. Muscat, V. Swamy and N. Harrison, *Phys. Rev. B: Condens. Matter*, 2002, **65**, 224112–224127.
52 C. Han, R. Luque and D. D. Dionysiou, *Chem. Commun.*, 2012, **48**, 1860–1862.
53 Y. Xie, S. H. Heo, Y. N. Kim, S. H. Yoo and S. O. Cho, *Nanotechnology*, 2010, **21**, 015303.
54 J. I. Goldstein, D. E. Newbury, P. Echlin, D. C. Joy, A. C. Romig, C. E. Lyman, C. Fiori and E. Lifshin, *Scanning Electron Microscopy and X-Ray Microanalysis*, Plenum Press, New York, 1992.
55 T. Bark and J. M. K. Nowotny, *J. Chem. Phys. B*, 2006, **110**, 21560–21567.
56 (*a*) M. K. Nowotny, T. Bark and J. Nowotny, *J. Chem. Phys. B*, 2006, **110**, 16302–16308; (*b*) J. Nowotny, *Oxide semiconductors for solar energy conversion: titanium dioxide*, Taylor & Francis Gourp, Boca Raton, 2012, pp. 145–147; (*c*) J. B. Moser, R. N. Blumenthal and D. H. Whitomore, *J. Am. Ceram. Soc.*, 1965, **48**, 384; (*d*) D.-K. Lee, L.-L. Jeon, M.-H. Kim, W. Choi and H.-I. Yoo, *Proc. Br. Ceram. Soc.*, 1967, **8**, 231–245.
57 D. L. Golic, Z. Brankovic, N. Daneu, S. Bernik and G. Brankovic, *J. Sol-Gel Sci. Technol.*, 2012, **63**, 116125.
58 R.-Q. Song and H. Cölfen, *Adv. Mater.*, 2010, **22**, 1301–1330.
59 L. Zhou and P. O'Brien, *J. Phys. Chem. Lett.*, 2012, **3**, 620–628.
60 A. Pottier, C. Chanéac, E. Tronc, L. Mazerolles and J.-P. Jolivet, *J. Mater. Chem.*, 2001, **11**, 1116–1121.
61 M. H. Yang, P. C. Chen, C. Tsai Mi, T. Ting Chen, I. C. Chang, H. T. Chiu and C. Y. Lee, *CrystEngComm*, 2014, **16**, 441–447.
62 M. R. Ranade, A. Navrotsky, H. Z. Zhang, J. F. Banfield, S. H. Elder, A. Zaban, P. H. Borse, S. K. Kulkarni, G. S. Doran and H. J. Whitfield, *Proc. Natl. Acad. Sci. U. S. A.*, 2002, **99**, 6476–6481.
63 S. Kalathil, M. M. Khan, S. A. Ansari, J. Lee and M. H. Cho, *Nanoscale*, 2013, **5**, 6323–6326.
64 K. F. Moura, J. Maul, A. R. Albuquerque, G. P. Casali, E. Longo, D. Keyson, A. G. Souza, J. R. Sambrano and I. M. G. Santos, *J. Solid State Chem.*, 2014, **210**, 171–177.
65 (*a*) A. T. Paxton and L. Thiên-Nga, *Phys. Rev. B: Condens. Matter*, 1998, **57**, 13233–13241; (*b*) W. Wunderlich, L. Miao, M. Tanemura, S. Tanemura, P. Jin, K. Kaneko, A. Terai, N. Nabatova-Gabin and R. Belkada, *Int. J. Nanosci.*, 2004, **3**, 439–445.

66 E. Longo, E. Orhan, F. M. Pontes, C. D. Pinheiro, E. R. Leite, J. A. Varela, P. S. Pizani, T. M. Boschi, F. Lanciotti Jr., A. Beltrán and J. Andrés, *Phys. Rev. B: Condens. Matter*, 2004, **69**, 125115.
67 L. Brus, *J. Phys. Chem.*, 1986, **90**, 2555–2560.
68 S. Feng and R. Xu, *Acc. Chem. Res.*, 2001, **34**, 239–247.
69 C. Bae, H. Yoo, M. Kim, S. Lee, H. Kim, T. K. Ahn and H. Shin, *J. Phys. Chem. C*, 2014, **118**, 9726–9732.
70 (*a*) G. Pirug, C. Ritke and H. P. Bonzel, *Surf. Sci.*, 1991, **241**, 289–301; (*b*) B. Erdem, R. A. Hunsicker, G. W. Simmons, E. D. Sudol, V. L. Dimonie and M. S. El-Aasser, *Langmuir*, 2001, **17**, 2664–2669.
71 (*a*) M. Murata, H. Wakino and S. Ikeda, *J. Electron Spectrosc. Relat. Phenom.*, 1975, **6**, 459–464; (*b*) C. Gao, H. Song, L. Hu, G. Pan, R. Qin, F. Wang, Q. Dai, L. Fan, L. Liu and H. Liu, *J. Lumin.*, 2008, **128**, 559–564; (*c*) C. D. Wagner, W. M. Riggs, L. E. Davis, J. F. Moulder and G. E. Muilenberg, *Handbook of X-ray photoelectron spectroscopy: a reference book of standard data for use in x-rayphotoelectron spectroscopy*, Perkin-Elmer MN, Eden-Prairie, 1979; (*d*) Q. Xiao, L. Ouyang, L. Gao and W. Jiang, *Mater. Chem. Phys.*, 2010, **124**, 1210–1215.
72 L.-B. Xiong, J.-L. Li, B. Yang and Y. Yu, *J. Nanomater.*, 2012, 831524.
73 (*a*) P. Villards and C. D. Calvert, *Pearson's Handbook of Crystallographic Data for Intermetallic Phases*, American Society of Metals, Metals Park, OH, 1985; (*b*) A. F. Carley, P. R. Chalker, J. C. Rivieret and M. W. Roberts, *J. Chem. Soc., Faraday Trans. 1*, 1987, **83**, 351–370; (*c*) W. Zhang, Y. Li, S. Zhu and F. Wang, *Chem. Phys. Lett.*, 2003, **373**, 333–337; (*d*) S. Hashimoto and A. Tanaka, *Surf. Interface Anal.*, 2002, **34**, 262–265.
74 D. Regonini, A. Jaroenworaluck, R. Stevens and C. R. Bowena, *Surf. Interface Anal.*, 2010, **42**, 139–144.
75 J. F. Moulder, W. F. Stickle, P. E. Sobol and K. D. Bomben, *Handbook of X-Ray Photoelectron Spectroscopy*, Perkin-Elmer Corp., Eden Prairie, Minnesota, 1992.
76 A. Iwabuchi, C. Choo and K. Tanaka, *J. Phys. Chem. B*, 2004, **108**, 10863–10871.
77 R. Wang, N. Sakai, A. Fujishima, T. Watanabe and K. Hashimoto, *J. Phys. Chem. B*, 1999, **103**, 2188–2194.
78 J. P. Knauth and H. L. Tuller, *J. Appl. Phys.*, 1999, **85**, 897–902.
79 (*a*) G. Redmond, D. Fitzmaurice and M. Graetzel, *J. Phys. Chem.*, 1993, **97**, 6951–6954; (*b*) G. Lu, A. Linsebigler and J. T. Yates, *J. Phys. Chem.*, 1994, **98**, 11733–11738.
80 Y. Cao, Z. Zhao, J. Yi, C. Ma, D. Zhou, R. Wang, C. Li and J. Qiu, *J. Alloys Compd.*, 2013, **554**, 12–20.
81 (*a*) A. R. Albuquerque, A. Bruix, I. M. G. dos Santos, J. R. Sambrano and F. Illas, *J. Phys. Chem. C*, 2014, **118**(18), 9677–9689; (*b*) A. R. Albuquerque, J. Maul, E. Longo, I. M. G. dos Santos and J. R. Sambrano, *J. Phys. Chem. C*, 2013, **117**(14), 7050–7061; (*c*) C. Di Valentin and A. Selloni, *J. Phys. Chem. Lett.*, 2011, **2**(17), 2223–2228.
82 (*a*) E. Longo, E. Orhan, F. M. Pontes, C. D. Pinheiro, E. R. Leite, J. A. Varela, P. S. Pizani, T. M. Boschi, F. Lanciotti, A. Beltrán Jr. and J. Andrés, *Phys. Rev. B: Condens. Matter*, 2004, **69**, 125115; (*b*) J. C. Sczancoski, L. S. Cavalcante, M. R. Joya, J. W. M. Espinosa, P. S. Pizani, J. A. Varela and E. Longo, *J. Colloid Interface Sci.*, 2009, **330**, 227–236; (*c*) V. M. Longo, L. S. Cavalcante, E. C. Paris, J. C. Sczancoski, P. S. Pizani, M. S. Li, J. Andrés, E. Longo and J. A. Varela, *J. Phys. Chem. C*, 2011, **115**, 5207–5219.
83 J. Marzin, J. Gérard, A. Izraël, D. Barrier and G. Bastard, *Phys. Rev. Lett.*, 1994, **73**, 716–719.
84 N. Greenham, X. Peng and A. Alivisatos, *Phys. Rev. B: Condens. Matter*, 1996, **54**, 17628–17637.
85 S. J. L. Billinge and I. Levin, *Science*, 2007, **316**, 561–565.
86 (*a*) Y. Lei, L. D. Zhang, G. W. Meng, G. H. Li, X. Y. Zhang, C. H. Liang, W. Chen and S. X. Wang, *Appl. Phys. Lett.*, 2001, **78**, 1125–1127; (*b*) J. C. Yu, J. Yu, W. Ho, Z. Jiang and L. Zhang, *Chem. Mater.*, 2002, **14**, 3808–3816; (*c*) N. Wang, H. Lin, X. Yang and L. Zhang, *J. Lumin.*, 2007, **122**, 889–891; (*d*) N. Serpone, D. Lawless and R. Khairutdinov, *J. Phys. Chem.*, 1995, **99**, 16646–16654.
87 http://www.systat.com/products/PeakFit/.
88 L. V. Saraf, S. I. Patil, S. B. Ogale, S. R. Sainkar and S. T. Kshirsager, *Int. J. Mod. Phys. B*, 1998, **12**, 2635–2647.
89 L. Forss and M. Schubnell, *Appl. Phys. B*, 1993, **56**, 363–366.
90 V. M. Longo, A. T. de Figueiredo, A. B. Campos, J. W. M. Espinosa, A. C. Hernandes, C. A. Taft, J. R. Sambrano, J. A. Varela and E. Longo, *J. Phys. Chem. A*, 2008, **112**, 8920.
91 L. S. Cavalcante, E. A. V. Ferri, J. C. Sczancoski, E. C. Paris, J. W. M. Espinosa, A. T. de Figueiredo, P. S. Pizani, V. R. Mastelaro, J. A. Varela and E. Longo, *Mater. Chem. Phys.*, 2009, **117**, 192–198.
92 K. Momma and F. Izumi, *J. Appl. Crystallogr.*, 2011, **44**, 1272–1276.
93 L. S. Cavalcante, A. Z. Simões, J. W. M. Espinosa, L. P. S. Santos, E. Longo, J. A. Varela and P. S. Pizani, *J. Alloys Compd.*, 2008, **464**, 340–346.
94 Y. Toyozawa, Elementary Processes in Luminescence, *J. Lumin.*, 1976, 12–13.
95 W. A. Weyl and T. Forland, *Ind. Eng. Chem.*, 1950, **42**, 257–263.
96 L. F. da Silva, W. Avansi Jr., J. Andrés, C. Ribeiro, M. L. Moreira, E. Longo and V. R. Mastelaro, *Phys. Chem. Chem. Phys.*, 2013, **15**, 12386–12393.
97 V. Kumar, V. Kumar, S. Som, J. H. Neethling, M. Lee, O. Ntwaeaborwa and H. C. Swart, *Nanotechnology*, 2014, **25**, 135701.